1   **Structure and ion-release mechanism of P$_{IB-4}$-type ATPases**
2

3   Christina Grønberg[1], Qiaoxia Hu[1], Dhani Ram Mahato[2], Elena Longhin[1], Nina
4   Salustros[1], Annette Duelli[1], Pin Lyu[1], Viktoria Bågenholm[1], Jonas Eriksson[2], Komal
5   Umashankar Rao[3], Domhnall Iain Henderson[3], Gabriele Meloni[4], Magnus
6   Andersson[2], Tristan Croll[5], Gabriela Godaly[3], Kaituo Wang[1] and Pontus Gourdon[1,6]

7

8   [1] Department of Biomedical Sciences, University of Copenhagen, Blegdamsvej 3B,
9   Copenhagen N, 2200, Denmark
10   [2] Department of Chemistry, Umeå University, Linneaus Väg 10, 901 87 Umeå,
11   Sweden
12   [3] Department of Laboratory Medicine, Lund University, Klinikgatan 28, Lund, 222 42,
13   Sweden
14   [4] Department of Chemistry and Biochemistry, The University of Texas at Dallas, 800
15   W Campbell Rd., Richardson, TX 75080, USA
16   [5] Cambridge Institute for Medical Research, Department of Haematology, University
17   of Cambridge, Keith Peters Building, Hills Rd, Cambridge CB2 0XY, United
18   Kingdom
19   [6] Department of Experimental Medical Science, Lund University, Sölvegatan 19,
20   Lund, 221 84, Sweden

21

22   **Abstract**

23   **Transition metals, such as zinc, are essential micronutrients in all organisms, but**
24   **also highly toxic in excessive amounts. Heavy-metal transporting P-type (P$_{IB}$)**
25   **ATPases are crucial for homeostasis, conferring cellular detoxification and**
26   **redistribution through transport of these ions across cellular membranes. No**
27   **structural information is available for the P$_{IB-4}$-ATPases, the subclass with the**
28   **broadest cargo scope, and hence even their topology remains elusive. Here we**
29   **present structures and complementary functional analyses of an archetypal**
30   **P$_{IB-4}$-ATPase, sCoaT from *Sulfitobacter sp. NAS14-1*. The data disclose the**
31   **architecture, devoid of classical so-called heavy metal binding domains, and**
32   **provides fundamentally new insights into the mechanism and diversity of heavy-**
33   **metal transporters. We reveal several novel P-type ATPase features, including a**
34   **dual role in heavy-metal release and as an internal counter ion of an invariant**

histidine. We also establish that the turn-over of P_{IB}-ATPases is potassium independent, contrasting to many other P-type ATPases. Combined with new inhibitory compounds, our results open up for efforts in e.g. drug discovery, since P_{IB-4}-ATPases function as virulence factors in many pathogens.

Introduction

The ability to adapt to environmental changes in heavy metal levels is paramount for all cells, as these elements are essential for a range of cellular processes and yet toxic at elevated concentrations[1, 2]. Transition metal transporting P-type (P_{IB}) ATPase proteins are critical for cellular heavy metal homeostasis, providing efflux of e.g. copper, zinc and cobalt from the intracellular milieu. Indeed, malfunctioning of the human P_{IB}-members, ATP7A and ATP7B, cause the fatal neurological Menkes disease and Wilson disease [3, 4]. The P_{IB}-ATPases belong to the P-type ATPase superfamily of integral membrane proteins, which exploit energy from ATP hydrolysis for transport of cargo across cellular membranes. These proteins share an overall mechanism described by the so-called Post-Albers cycle[5, 6], as established by decades of structural and functional investigations of primarily Ca^{2+}-, Na^+/K^+- and H^+-specific P-type ATPases[7-15]. In summary, four cornerstone states, E1-E1P-E2P-E2, provide alternating access and affinity for the transported ions (and counter-ions, if present). Inward facing (e.g. cytosolic) E1 and outward facing (e.g. extracellular) E2P conformations are coupled to ATP-dependent phosphorylation (yielding ion-occluded E1P) and dephosphorylation (to occluded E2) of an invariant catalytical aspartate, respectively.

P_{IB}-ATPases are subdivided into groups based on conserved sequence motifs and the selectivity towards transported transition metal ions[16-19]. Whereas Cu^+- and Zn^{2+}-transporting P_{IB-1} and P_{IB-2} ATPases are relatively well-characterized, little is known regarding the P_{IB-4} proteins, which comprise some of the simplest and shortest proteins within the entire P-type ATPase superfamily[16]. They are present in plants, archaea and prokaryotes, and have been assigned a role as virulence factors in pathogens, as e.g. the P_{IB-4}-ATPase MtCtpD is required for tuberculosis infections [20, 21], and therefore represent attractive targets for novel antibiotics.

The P_{IB-4}-ATPases are classically referred to as cobalt transporters. However, the metal specificity of the P_{IB-4} ATPases remain elusive as some members have a confirmed cobalt-specificity, while others seemingly have broader or altered ion-

69 transport profiles, also transporting ions such as Zn^{2+}, Ni^{2+}, Cu^+ and even Ca^{2+} [18, 22-

70 25]. Thus, the P_{IB-4}-ATPases appear to have the widest scope of transported ions of the

71 P_{IB}-ATPases, and it is possible that further sub-classification principles and sequence

72 motifs will be identified. Due to the broad ion transport range, they have been

73 proposed to serve as multifunctional emergency pumps that can be exploited under

74 extreme environmental stress to maintain heavy metal homeostasis[26].

75 Hitherto, the available high-resolution structural information of full-length P_{IB}-

76 ATPases is limited to two structures each of ion-free conformations of the Cu^+-

77 transporting P_{IB-1}-ATPase from *Legionella pneumophila* (LpCopA)[27, 28], and the

78 Zn^{2+}-transporting P_{IB-2}-ATPase from *Shigella sonnei* (SsZntA)[28]. Thus, the principal

79 architecture of the P_{IB-4}-ATPases remains debated, as sequence analyses have

80 proposed different topologies for the N-terminus: with or without i) the so-called

81 called heavy metal binding domains (HMBDs), and ii) the first two transmembrane

82 helices, MA and MB [16, 29-31], which both are present in other P_{IB}-ATPases (**Figure 1**

83 **– figure supplement 1a**). These represent structural features that have been suggested

84 to be important for ion-uptake and/or regulation in other P_{IB}-ATPases[27, 28, 32, 33],

85 raising questions if similar levels of protein control are absent or replaced in the P_{IB-4}

86 group. In addition, despite a shared overall architecture, the P_{IB-1} and P_{IB-2} structures

87 suggested significantly different types of entry and exit pathways, hinting at unique

88 translocation mechanisms for each P_{IB} group [34] . However, it remains unknown if

89 similar molecular adaptions have taken place in P_{IB-4}-ATPases to handle the unique

90 array of cargos. To address these fundamental questions, we determined structures of

91 a P_{IB-4}-ATPase in different states and validated our findings using *in vitro* functional

92 characterization.

93

94 **Results & Discussion**

95 **Metal specificity**

96 We employed the established P_{IB-4} model sCoaT (UniProt ID A3T2G5) to shed

97 further light on the structure and mechanism of the entire P_{IB-4}-class. As the metal ion

98 specificity of the P_{IB-4}-ATPases is known to be wide, the ATPase activity was

99 assessed *in vitro* in lipid-detergent solution using the so-called Baginski assay, in the

100 presence of a range of different heavy metals. The protein exhibited clear Zn^{2+} and

101 Cd^{2+} dependent ATPase activity, while Co^{2+} only stimulated ATP-hydrolysis at high

102 ion concentrations (**Figure 2 – figure supplement 1**). This is in partial agreement

103   with the ion range profile previously reported for sCoaT, as higher Co^{2+} sensitivity

104   has been detected using a different functional assay and different experimental

105   conditions[18] (**Figure 2 – figure supplement 1**).

106   The fact that the K_M value for the Co^{2+}-dependent sCoaT activity reported previously

107   is lower than measured in this study is unexpected (**Figure 2 – figure supplement**

108   **1b**)[18]. We therefore assessed if this observation relates to lower available

109   concentration of Co^{2+} consequent to chelation by buffer solution components, or if

110   this metal interferes with the color development in the ATPase assays determining P_i

111   concentrations (**Figure 2 – figure supplement 1c**). However, Co^{2+} and Zn^{2+} display

112   similar Baginski color development as determined by calibration with separate

113   standard curves. Moreover, neither exclusion of azide and molybdate to avoid

114   possible Co^{2+}-binding of these compounds, nor supplementation of the reducing agent

115   TCEP (to avoid possible oxidation of Co^{2+} from molecular oxygen) has a significant

116   effect on turn-over. We also investigated if the type of assay may affect the outcome

117   (**Figure 2 – figure supplement 1c**). However, employment of the alternative

118   Malachite Green Phosphate Assay essentially reproduced the relative activity in the

119   presence of Zn^{2+} and Co^{2+}, respectively[35]. sCoaT is purified in a buffer containing 5

120   mM β-mercaptoethanol, and even following dilution into the assay buffer the

121   concentration is still approximately 100 µM, and as thiols can act as ligands for Co^{2+}

122   it may explain part of the differences in the K_M values. However, this still does not

123   explain why Zn^{2+} and Cd^{2+} dependent ATPase activity has not been observed for

124   sCoaT in the previously study [26], although other P_{IB-4}-members have been associated

125   with Zn^{2+}-activity. While not detected, the reported K_M and V_{max} may nevertheless be

126   influenced by numerous environmental factors not tested for here, such as lipids,

127   detergents, presence/absence/location of metal-binding his-tags or other settings.

128   Despite that higher sensitivity has been measured for Zn^{2+} compared to Co^{2+}, it cannot

129   be excluded that Co^{2+}, rather than Zn^{2+}, is the preferred cargo *in vivo* as the relative

130   intracellular availability of Co^{2+} is more than three orders of magnitude higher than

131   that of Zn^{2+} in certain bacterial cells[36].

132

133   **Structure determination**

134   We determined structures of sCoaT in metal-free conditions supplemented with two

135   different phosphate analogues, BeF_3^- and AlF_4^-, respectively, which previously have

136   been exploited to stabilize E2 reaction intermediates of the transport cycle of P_{IB-}

137 ATPases[28, 37, 38]. The structures were determined at 3.1 Å and 3.2 Å resolution, using

138 molecular replacement as phasing method and SsZntA as search model, and the final

139 models yielded R/R_{free} of 24.4/26.8 and 21.8/25.5 (**Table 1**). The two crystal forms

140 were obtained using the HiLiDe method (crystallization in the presence of high

141 concentrations of detergent and lipids)[39]. Surprisingly however, the crystal packing

142 for both structures reveal only minor contacts between adjacent membrane-spanning

143 regions, which are critical for the crystals obtained of most other P-type ATPase

144 proteins[28, 37, 40] (**Figure 1 – figure supplement 2**). Hence, some crystal forming

145 interactions likely take place through lipid-detergent molecules. To our knowledge,

146 this is the first time that type I crystals with unrestrained transmembrane domains are

147 reported, but a consequence is that peripheral parts of the membrane domain are less

148 well-resolved (**Figure 1 – figure supplement 3**). While this caused difficulty in

149 modelling some transmembrane (TM) helices, satisfying solutions were found with

150 the aid of the software ISOLDE[41] due to its use of AMBER forcefield which helped

151 to maintain physical sensibility in the lowest-resolution regions. In addition, root

152 means square deviation, secondary structure as well as centers-of-mass of the

153 transmembrane helices, only showed minor variation over time in MD simulations,

154 indicative of a stable structure (**Figure 1 – figure supplement 4-5**). The TM helices

155 also showed lowered backbone root mean square fluctuation compared to more

156 dynamic regions, such as the soluble domains and loop regions (**Figure 1 – figure**

157 **supplement 4b**).

158

159 **Overall structure, without classical HMBD**

160 Examination of the structures reveals that the P_{IB-4}-ATPase architecture is reminiscent

161 to that of other P-type ATPases, with three cytosolic domains, A (actuator), N

162 (nucleotide-binding) and P (phosphorylation), as well as a membrane spanning M-

163 domain (**Figure 1a**). Furthermore, the core of the soluble portions, including the

164 nucleotide binding pocket and catalytic phosphorylation site at D369, are well-

165 conserved.

166 The topology of P_{IB-4}-ATPases has been a conundrum as sequence analyses have

167 proposed different arrangements, with variable number of transmembrane segments

168 and different sizes of the N-termini [16, 27, 28, 30, 31, 38]. However, our data

169 unambiguously demonstrate that P_{IB-4}-ATPases possess eight transmembrane helices,

170 MA and MB followed by M1-M6. As previously observed for P_{IB-1}- and P_{IB-2}-

171   ATPases, MB is kinked by a conserved Gly-Gly motif (G82 and G83), forming an
172   amphipathic 'platform', MB', immediately prior to M1, see further below (**Figure 1 –**
173   **figure supplement 3)**.
174   Are then HMBDs present in P_{IB-4}-ATPases as in the other P_{IB} subclasses? As only the
175   first 47 residues remain un-modelled in the final structures (**Supplementary Table**
176   **1**), it is clear that many P_{IB-4}-ATPases including sCoaT are lacking a classical HMBD
177   ferredoxin-like fold (typically 70 residues long). In agreement with this observation,
178   the cysteine pair (CGIC in the sequence) in the N-terminus of sCoaT is rather
179   positioned in MA, facing M1 (**Figure 1 – figure supplement 1, 3**), in contrast to the
180   surface-exposed, metal-binding CXXC hallmark-motif detected in classical HMBDs.
181   Functional analysis of mutant forms lacking these cysteines *in vitro* also support that
182   they are unimportant for function (**Figure 2a**). We note that there are P_{IB-4}-ATPases
183   with extended N-termini that, in contrast to sCoaT, may harbour HMBDs[16].
184   Conversely, the sCoaT N-terminus is rich in metal-binding methionine, cysteine,
185   histidine, aspartate and glutamate residues, and this feature is conserved among P_{IB-4}-
186   ATPases (**Figure 2 – figure supplement 2**). We therefore explored the role of this N-
187   terminal tail through assessment of an sCoaT form lacking the first 33 residues.
188   However, *in vitro* characterization suggests only minor differences compared to wild-
189   type, indicating that the residues upstream of MA are not essential for catalytic
190   activity (**Figure 2a**). Aggregated, this hints at that no classical HMBD is present, and
191   hence that this level of regulation is absent in many P_{IB-4}-ATPases, although it cannot
192   be excluded that the N-termini are important *in vivo*.
193   Interestingly, it has been shown that the *in vivo* transport specificity of the sCoaT
194   homolog from *Synechocystis PCC 6803* (CoaT) can be switched from Co^{2+} to Zn^{2+} by
195   exchanging the N-terminal region to that of the Zn^{2+} transporting P_{IB-2} ATPase ZiaA
196   from same organism [42]. This demonstrates that P_{IB-4}-ATPases not only *in vitro* (our
197   data), but also *in vivo* are able to transport Zn^{2+}, if the M-domain gain access to the
198   metal. One possible explanation for the change of specificity for the CoaT chimeric
199   construct, is that the N-terminal peptide tail, as also suggested for ATP7B[43], prevents
200   ATP hydrolysis through binding to the soluble domains, and this inhibition is then
201   released upon binding of the cognate metal to the N-terminal and/or HMBD.
202   However, it is also possible that the role of the N-terminal region of P_{IB-4}-proteins is
203   to impair Zn^{2+} acquisition, an ability that is lost when exchanged with the N-terminal
204   part of ZiaA. Preliminary assessment of the metal specificity influence of the N-

205 terminal tail of sCoaT suggest it has little or no effect on distinguishing between Co^{2+}

206 and Zn^{2+} *in vitro* (**Figure 2 – figure supplement 1d**). From this it is clear that further

207 studies are needed to shed light on the function of the N-terminal region in P_{IB}-

208 ATPases, also in P_{IB-4}-ATPases.

209 Associated, this raises questions also on the role of the above-mentioned MB'

210 platform, which has been proposed to serve as an interaction site for HMBDs in P_{IB-1}-

211 and P_{IB-2}-ATPases, and for the Cu^+-ATPases as a docking site for metal delivering

212 chaperones[27, 28, 32, 44]. As there are no known zinc/cadmium chaperones for P_{IB-4}-

213 ATPases, and because classical HMBDs appear to be missing in at least some

214 proteins of the group, the MB' function may need to be revisited. Alternatively, the

215 N-terminus may have merely been maintained through evolution without conferring

216 functional benefits or disadvantages.

217

218 **Structures in a transition state of dephosphorylation**

219 The classical view of P-type ATPases is that the E2P state is outward-open and that

220 the following transition state of dephosphorylation, $E2.P_i$, is occluded, and that these

221 conformations can be stabilized using the phosphate analogues employed here for

222 structure determination, BeF_3^- and AlF_4^-, respectively. Furthermore, distinct ion

223 release pathways have been proposed among P_{IB}-ATPases[27-29, 45], including a narrow

224 exit pathway lined by MA, M2 and M6 that remains open also in the $E2.P_i$ state for

225 the P_{IB-1}-ATPases. In contrast, a wide opening extending from the location of the

226 bound metal in the M-domain of ion-occluded states to the non-cytoplasmic side has

227 been observed for the P_{IB-2}-ATPases, and this group becomes re-occluded with the

228 E2P to $E2.P_i$ shift.

229 Surprisingly however, analysis of the two obtained structures suggests that the

230 anticipated significant domain reorientations are absent in sCoaT (**Figure 2b**), and the

231 models are in contrast rather similar. The compact assembly of the soluble domains

232 and the position of the A-domain near the P-domain, placing the conserved TGE-

233 motif responsible for dephosphorylation towards the phosphorylation site, are

234 typically associated with commencement of dephosphorylation, indicating that the

235 two structures are trapped in an $E2.P_i$ like transition state (**Figure 2 – figure**

236 **supplement 3a-c, e**). This observation differs from the equivalent structures of the

237 other structurally determined P_{IB}-ATPases, in which the phosphorylation site of the

238 E2P state (stabilized by BeF_3^-) is shielded from the TGE-loop as also observed for the

239   well-studied sarcoendoplasmic reticulum Ca^{2+}-ATPase (SERCA) (**Figure 2 – figure**

240   **supplement 3d)**.

241   Notably, analogous highly similar BeF_3^-- and AlF_4-stablized structures have recently

242   also been observed for the Ca^{2+}-specific P-type ATPase from *Listeria monocytogenes*

243   (LMCA1)[46]. It was proposed that LMCA1 pre-organizes for dephosphorylation

244   already in a late E2P state (E2P*, stabilized by BeF_3^-), in accordance with its rapid

245   dephosphorylation. Favoured occlusion and activation of dephosphorylation directly

246   upon ion-release may thus also be the case for sCoaT, and consequently the $E2-BeF_3^-$

247   structure captured here may represents a late (or quasi) E2P state (E2P*).

248   Comparisons of the sCoaT structures to the equivalent structure of SsZntA ($E2.P_i$)

249   revealed a unique arrangement of the A-domain (**Figure 2 – figure supplement 4**).

250   The TGE-loop region superposes well with the corresponding area in SsZntA, but the

251   rest of the A-domain is rotated towards the P-domain - approximately 14° and 5.3 Å

252   (**Figure 2 – figure supplement 4**). However, it cannot be excluded that this rotation

253   is due to crystal contacts as the two peripheral β-sheets of the A-domain are

254   interacting tightly with parts of a neighbouring molecule. Additionally, we noticed

255   that the A-domain of sCoaT possesses a surface-exposed extension similar to

256   SERCA, but this feature is not present in P_{IB-1}- and P_{IB-2}-ATPases and it is not a

257   conserved property in the P_{IB-4}-group either (**Figure 2 – figure supplement 2, 4**).

258   Conversely, the M-domains of the two sCoaT structures are overall similar and appear

259   outward-occluded (**Figure 2c**), as also supported by comparisons with the equivalent

260   structures of SsZntA, again contrasting to the situation observed in P_{IB-1}- and P_{IB-2}-

261   ATPases.

262

263   **Ion-release**

264   Next, to shed light on ion-release, we compared the sCoaT structures to the E2P state

265   of SsZntA, in which the extracellular ends of M5 and M6 shift away from the

266   proposed metal binding site, allowing an exit pathway to be formed (**Figure 2d**).

267   Considering that P_{IB-2}- and P_{IB-4}-ATPases have overlapping cargo range, share overall

268   topology and that they release ions in free-form to the extracellular environment, in

269   contrast to their P_{IB-1}-counterparts, we find it likely that they employ similar exit

270   pathways, lined primarily by M2, M4, M5 and M6 (**Figure 2d**)[28, 38].

271   The high affinity binding site in P_{IB-4} ATPases has previously been suggested to be

272   formed by residues from the conserved SPC- (starting from S325) and HEGxT- (from

273   H657) motifs of M4 and M6, based on X-ray absorption spectroscopy (XAS) and

274   mutagenesis studies[18, 47]. An outstanding remaining question is, however, how the

275   ion is then discharged to the extracellular site? Among the resides that likely

276   constitute the high affinity binding site, remarkably E658 of M6 is pointing away

277   from the ion-binding region around the SPC motif (**Figure 2e and Figure 1 – figure**

278   **supplement 3**). We anticipate that E658 rotates away from its ion-binding

279   configuration in the E1P to E2P transition, thereby assisting to lower the cargo-

280   affinity to permit release via the M2, M4, M5 and M6 cavity (**Figure 2e**). The

281   conserved E120 of M2 (sometimes replaced with an aspartate in P_{IB-4}-ATPases) is

282   located along this exit pathway. The residue also overlays with the conserved E202 in

283   SsZntA (**Figure 2f**), which has been suggested to serve as a transient metal ligand,

284   stimulating substrate release from the CPC motif of P_{IB-2}-ATPases[28]. We propose a

285   similar role for E120 in sCoaT as further supported by the decreased activity of

286   E120A sCoaT form (**Figure 2a**).

287

288   **A unique internal counter-ion principle**

289   Many P-type ATPases couple ion- and counter-transport, and hence the reaction cycle

290   cannot be completed without counter-ions. The importance of the counter-transport

291   has been demonstrated in e.g. Ca^{2+}/H^+- (such as SERCA), Na^+/K^+- and H^+/K^+-

292   ATPases [48-51]. In contrast, absence of counter-transport has been proposed for P_{IB-2}-

293   ATPases[28], H^+-ATPases[52] and P4-ATPases[53], which rather exploit a built-in

294   counter-ion Specifically for the P_{IB-2}-ATPases, a conserved lysine of M5 (K693 in

295   SsZntA) serves as the counter ion, through interaction with the conserved metal

296   binding aspartate of M6 (D714 in SsZntA) in E2 states. Similarly, P_{IB-1}-ATPases are

297   not Cu^+/H^+ antiporters, but a likely built-in counter-ion residue is not conserved in the

298   group[54]. Instead, it is possible that the requirement for counter-ion translocation is

299   prevented by the narrow exit pathway, preventing back-transfer of the released ion

300   and perhaps rendering complete-occlusion unnecessary [54]. For the P_{IB-4}-ATPases,

301   biochemical studies have proposed an ion-binding stoichiometry of one [18, 22, 26, 47],

302   however no information is available regarding the presence or absence of counter

303   transport.

304   In the E2-BeF$_3^-$ sCoaT structure, we identify a tight configuration of HEGxT-motif

305   H657, being sandwiched between the SPC residues, distinct from the M5 lysine - M6

306   aspartate interaction observed in P$_{IB-2}$-ATPases (**Figure 2g-h**). Despite the packing

307   issues of the generated crystals, clear electron-density is visible for H657, indicating a

308   rigid conformation (**Figure 2g**). Moreover, activity measurements of an alanine

309   substitution of H657 demonstrate that it is crucial for function (**Figure 2a**). In light of

310   these findings and an earlier report suggesting that a mutation of the equivalent of

311   H657 in MtCtpD leaves the ion affinity unaffected[47], we suggest this histidine serves

312   as an internal counter-ion, similarly as for the invariant lysine in SsZntA, perhaps

313   preventing back-transfer of released ions and for charge stabilization, however we

314   cannot exclude that H657 is also part of the high affinity binding site in sCoaT.

315   The rigid conformation observed for H657 in the E2-BeF$_3^-$ structure is also observed

316   in the E2-AlF$_4^-$ structure (**Figure 1 – figure supplement 3b**). In contrast, for SsZntA

317   the interaction between K693 and D714 is only detected in the E2.P$_i$ state. Thus, the

318   interaction pattern is consistent with the idea that sCoaT pre-organizes for

319   dephosphorylation already in the (late) E2P state, with the associated occlusion and

320   internal counter-ion interaction taking place earlier than for SsZntA.

321

A more potent A-domain modulatory site

323   A conserved K$^+$-site, which cross-links between the A- and P-domains in E2 states

324   and thereby allosterically stimulates the E2P to E2 process [55, 56], has been suggested

325   to be present also in P$_{IB}$-ATPases [55]. However, our new E2 structures and available

326   structures of P$_{IB-1}$- and P$_{IB-2}$-ATPases suggest that the A-/P-domain linker is

327   maintained without K$^+$ in P$_{IB}$-ATPases, and instead is established directly between

328   R273/D601 in sCoaT, as also supported by potassium titration experiments

329   monitoring sCoaT ATPase activity (**Figure 3a-d**). Nevertheless, the A-/P-domain

330   point-of-interaction appears critical for P$_{IB}$-ATPases, as functional characterization of

331   R273A, D601A and D601K result in a marked reduction of turn-over (**Figure 2a**).

332   This differs from similar mutations of classical P-type ATPases, where only minor

333   effects are observed [55, 56]. Furthermore, substitution of D601 with glutamate suggests

334   that even the A-/P-domain distance is critical (**Figure 2a**). It is possible that P$_{IB}$-

335   ATPases are more reliant on this particularly tight, ion-independent stabilization, as

336   the A-M1/A-domain linker is absent, and because many other P-type ATPases also

337   have a complementary A-/P-domain interaction (**Figure 1 – figure supplement 1c**).

338   Thus, our data indicate that this regulation is a general feature of many P-type ATPase

339   classes, yet featuring unique properties for P_{IB}-ATPases.

340

341   **New metal-transport blockers**

342   P_{IB-2}- and P_{IB-4}-ATPases serve as virulence factors and are critical for the disease

343   caused by many microbial pathogens, as underscored by the frequent presence of

344   several redundant genes[57-60]. In this light and because these P-type ATPases are

345   missing in humans, they represent putative targets for novel antibiotics. The shared

346   mechanistic principles identified here suggest that compounds can be identified that

347   inhibit both P_{IB}-groups, for example directed against the common release pathway,

348   thereby increasing efficacy. Indeed, screening of a 20,000-substance library using a

349   complementary *in vitro* assay, uncovers several compounds that abrogate function of

350   sCoaT and SsZntA (**Figure 3e-f**, data only shown for sCoaT). Furthermore, initial

351   tests of two of these suggest they have a potent effect against mycobacteria, which

352   previously have been shown to be P_{IB-4}-dependent for infection [47]; 90 % of the

353   mycobacteria were killed at mean concentrations of 18.75 and above 50 µM,

354   respectively, using either of these two separate molecules (**Figure 3g**). In contrast,

355   investigation of cytotoxic effects on primary human macrophages at concentrations

356   up to 25 µM demonstrated considerably less impact on cell survival for both blockers

357   (**Figure 3h**). Evidently downstream in-depth studies, ranging from investigations of

358   the target specificity, the detailed effect on human cells as well as antibiotic potency

359   in human, are required to fully understand the value of these putative P_{IB-2}- and P_{IB-4}-

360   inhibitors. Nevertheless, the substances outlined here represent promising leads for

361   drug-discovery efforts or to aid the development of tools to manipulate heavy metal

362   accumulation in plants to prevent accumulation or for enrichment.

363

364   **Conclusion**

365   Collectively, the first structure of a P_{IB-4}-type ATPase reveals the topology of P_{IB-4}-

366   ATPases, displaying an eight helix M-domain configuration, and likely no HMBDs,

367   at least in members without extended N-termini. Major findings include the

368   observation of an ion-release-pathway similar as in the related P_{IB-2}-ATPases, a

369   previously not observed counter-ion principle for P-type ATPases, and a unique

370   potassium-independent regulation of the P_{IB}-transport cycle (**Figure 4**). Thus, our

371   results significantly increase the understanding of heavy metal homeostasis in cells.

372   The novel identified putative inhibitors and the partially overlapping mechanistic

373   principles of P_{IB-2}- and P_{IB-4}-ATPases also open up a novel avenue for development of

374   compounds accessible from outside the cell against these P_{IB}-groups, to combat global

375   threats such as multi-drug resistance and/or tuberculosis or for biotechnological

376   purposes.

377 **Materials and methods**

378

Key Resources Table				
Reagent type (species) or resource	**Designation**	**Source or reference**	**Identifiers**	**Additional information**
Gene (*Sulfitobacter sp. (strain NAS-14.1))*	NAS141_02821	Synthetic	Uniprot: A3T2G5	
Cell line (*Escherichia coli*)	C41(DE3)	Sigma-Aldrich		Chemically competent cells
Cell line (*Mycobacterium bovis*)	BCG Montreal		ATCC 35735	
Software, algorithm	Phenix		RRID:SCR_014224	https://www.phenix-online.org/
Software, algorithm	ISOLDE	https://doi.org/10.1107/S2059798318002425		https://isolde.cimr.cam.ac.uk/
Software, algorithm	UCSF ChimeraX		RRID:SCR_015872	https://www.cgl.ucsf.edu/chimerax/
Software, algorithm	COOT		RRID:SCR_014222	http://www2.mrc-lmb.cam.ac.uk/personal/pemsley/coot/
Software, algorithm	Pymol		RRID:SCR_000305	http://www.pymol.org/

379

Overproduction and purification of sCoaT

380

381 Forms of the 72 kDa sCoaT from *Sulfitobacter sp. NAS14-1* (UniProt ID A3T2G5)

382 were transformed into *E. coli* (C41 strain) cells. The cells were cultured in LB

383 medium at 37 °C with shaking at 175 rpm in baffled flasks until the optical density

384 (600 nm) reached 0.6-1, cooled to 18 °C, and then induced with 1 mM IPTG for 16h.

385 Harvested cells were resuspended in buffer A (1 g cells per 5 mL buffer) containing

386 20 mM Tris-HCl, pH=7.6, 200 mM KCl, 20 % (v/v) glycerol and frozen at -80 °C

387 until further use. Cells were disrupted by two runs in a high-pressure homogenizer

388 (Constant System) at 25,000 psi following addition of 5 mM of fresh β-

389 mercaptoethanol (BME), 5 mM $MgCl_2$, 1 mM phenylmethanesulphonyl fluoride, 2

390 μg/mL DNase I and Roche protease inhibitor cocktail (1 tablet for 6 L cells). The

391 sample was kept at 4 °C throughout the purification. Cellular debris was pelleted via

392 centrifugation at 20,000 g for 20 minutes. Membranes were isolated by

393 ultracentrifugation for 3 h at 185,500 g, and resuspended in 10 mL buffer B (20 mM

394 Tris-HCl, pH=7.6, 200 mM KCl, 1 mM $MgCl_2$, 5 mM BME and 20 % (v/v) glycerol)

395 per g membranes and frozen at -80 °C until further use. The protein concentration in

396 the membranes was estimated using the Bradford assay[61]. Proteins were solubilized

397 through supplementation of 1 % (w/v) final concentration n-dodecyl-β-D-

398 maltopyranoside (DDM) and 3 mg/mL final total protein concentration in Buffer B

399 with gentle stirring for 2 h. Un-solubilized material was removed by

400 ultracentrifugation for 1 h at 185,500 g. The supernatant was supplemented with

401 imidazole to a final concentration of 30 mM and solid KCl (500 mM final

402 concentration), filtered (0.22 mm) and then applied to 5 mL HiTrap Chelating HP

403 columns (GE Healthcare, protein from 6 L cells per column) charged with Ni^{2+} and

404 equilibrated with 4 column volumes of buffer C (20 mM Tris-HCl, pH=7.6, 200 mM

405 KCl, 1 mM $MgCl_2$, 5 mM BME, 150 mg/mL octaethylene glycol monododecyl ether

406 ($C_{12}E_8$) and 20 % (v/v) glycerol). Proteins were eluted using a gradient, ending with

407 buffer C containing 500 mM imidazole. Eluted protein was assessed using SDS–

408 PAGE, and the fractions containing sCoaT concentrated to approximately 20 mg/mL

409 using VivaSpin concentrators (MWCO=50 kDa). 10 mg concentrated protein was

410 subjected to size-exclusion chromatography using a Superose 6 gel-filtration column

411 (GE-Healthcare), pre-equilibrated with 50 mL buffer E (20 mM Tris-HCl, pH=7.6, 80

412 mM KCl, 1 mM $MgCl_2$, 5 mM BME, 150 mg/mL $C_{12}E_8$ and 20 % (v/v) glycerol).

413 Fractions containing purified sCoaT were pooled, and concentrated to approximately

414   10 mg/mL, flash frozen in liquid nitrogen, and stored at -80 °C until further use. For

415   the experiments to assess K^+-dependence, the buffer E was replaced with 20 mM

416   Tris-HCl, pH=7.5, 1 mM $MgCl_2$, 5 mM BME, 0.15 mg/mL $C_{12}E_8$ and 20 % (v/v)

417   glycerol.

418

419   *Crystallization*

420   10 mg/mL sCoaT was supplemented with 3 mg/mL (final concentration) DOPC and 6

421   mg/mL (final concentration) $C_{12}E_8$, incubated at 4 °C and stirring for 16-48 h

422   (modified HiLiDe method[39]). Aggregates and insoluble DOPC were then removed

423   by ultracentrifugation at 50,000 g for 10 minutes. 2 mM $AlCl_3$ or $BeSO_4$, 10 mM NaF

424   and 2 mM EGTA (final concentrations) were supplemented and incubated on ice for

425   30 minutes. Crystals were grown using the hanging drop vapor diffusion method at

426   19 °C. E2-AlF_4^- crystals were grown with a reservoir solution containing 200 mM

427    $MgCl_2$, 14 % (v/v) PEG1500, 10 mM tris(2-carboxyethyl)phosphine, 10 % (v/v)

428   glycerol, 3 % 2-Methyl-2,4-pentanediol and 100 mM sodium acetate, pH=5.0. The

429   E2-BeF_3^- crystals were grown with a reservoir solution containing 200 mM

430   magnesium formate, 14 % (v/v) PEG5000, 100 mM sodium acetate, pH=4.0, and 0.5 %

431   (v/v) 2-propanol was added as an additive. Crystals were fished using litholoops

432   (Molecular Dimensions), flash-cooled in liquid nitrogen, and tested at synchrotron

433   sources. Complete final data sets were collected at the Swiss Light Source, the Paul

434   Scherrer Institute, Villigen, beam line X06SA.

435

436   *Structure determination and refinement*

437   Collected data were processed and scaled with XDS (**Supplementary Table 1**). For

438   the E2-AlF_4^- structure, initial phases were obtained by the molecular replacement

439   (MR) method using software PHASER [62] of the Phenix package [63], and using the

440   AlF_4^--stabilized structure of SsZntA (PDB ID: 4UMW) as a search model. The E2-

441   BeF_3^- structure was solved using the generated E2-AlF_4^- structure as a MR model.

442   Both crystal forms display poor crystal packing between the membrane domains

443   (**Figure 1 – figure supplement 2**), deteriorating the quality of the electron density

444   maps in these regions (**Figure 1 – figure supplement 3**). In this light, model building

445   of the membrane domains were executed with particular prudence, taking into

446   consideration the connectivity to the well-resolved soluble domains, distinct structural

447   features as well as sequence and structure conservation patterns. Examples of such

448   include the conserved GG motif that forms the kink in MB helix, which is clearly

449   identified also at low resolution, the SPC motif that twists the M4 helix and the

450   conserved and functionally important well-resolved residue H657 that assisted

451   assigning nearby residues.

452   Initial manual model building was performed primarily using COOT[64]. ISOLDE[65]

453   in ChimeraX[66] was employed for model building and analysis, and was critical for

454   obtainment of the final models with reasonable chemical restraints and low clash

455   score. In particular, ISOLDE's interactive register shifting tool was instrumental in

456   determining the register of the most weakly resolved TM helices. Secondary structure

457   restraints were applied in some flexible regions, also taking into consideration

458   homology to sCoAT and other models.

459   During final refinements with phenix.refine[67] the geometry was restrained in torsion

460   space to ISOLDE's output. Molprobity was exploited for structure validation[68]. The

461   final models are lacking the first 40 residues only, which is shorter than a classical

462   MBD of 67 amino acids. All structural figures were generated using Pymol[69].

463   Statistics for the final models were 96.70, 3.30, 0.20 and 0,74 for $E2-BeF_3^-$ and 93.24,

464   6.13, 0.63 and 8.31 for $E2-AlF_4^-$ in Ramachandran favored and allowed regions, and

465   for rotamer outliers and clash-score, respectively.

466

467   *Activity assay*

468   sCoAT forms were functionally characterized using the Baginski method to assess the

469   amount of released inorganic phosphate [70]. Briefly, 0.5 μg of purified sCoAT mixed

470   with reaction buffer containing 40 mM MOPS-KOH, pH=6.8, 5 mM KCl, 5 mM

471    $MgCl_2$, 150 mM NaCl, 0.3 mg/mL $C_{12}E_8$, 0.12 mg/mL soybean lipid, 5 mM NaN_3 and

472   0.25 mM Na_2MoO_4 in a total volume of 50 uL. For metal stimulation assays, different

473   heavy metal ions or EGTA was supplemented the reaction buffer to a final

474   concentration of 50 μM. For inhibitor screening (see how inhibitors were identified

475   below), different concentrations of inhibitors were added to the reaction buffer

476   containing 50 μM $ZnCl_2$. The samples were then incubated at 37 °C with 500 rpm

477   shaking for 5 minutes, and then supplemented with 5 mM ATP (final concentration)

478   to start the reaction, and incubated at 37 °C with 1000 rpm shaking for 10 mins. 50 μL

479   freshly prepared stop solution containing 2.5 % (w/v) ascorbic acid, 0.4 M (v/v) HCl

480   and 1 % SDS was then supplemented to stop the reaction and start color development.

481   75 μL color solution (2 % (w/v) arsenite, 2 % (v/v) acetic acid and 3.5 % (w/v)

sodium citrate) was added to the mixture following 10 minutes incubation at room temperature. Absorbance was measured at 860 nm after another 30 minutes incubation at room temperature. For the experiments to assess K^+-dependence, the reaction buffer was replaced with 40 mM Tris-HCl, pH=7.5, 5 mM $MgCl_2$, 3.0 mg/mL $C_{12}E_8$ and 1.2 mg/mL soybean lipid in a total volume of 50 uL.

Inhibitor screening

The inhibitor screening experiments were initially carried out on the zinc transporting P_{IB-2}-type ATPase ZntA from *Shigella sonnei* (SsZntA). SsZntA was produced and purified as described previously[28] and the inhibitory effect of approximately 20000 compounds was assessed by the Chemical biology Consortium Sweden (CBCS). Briefly, the ATPase activity of 0.7 μM highly pure protein was measured in the presence of 50 μM inhibitor through the release of inorganic phosphate (P_i) by the Baginski assay[70] in a total volume of 200 nL as reported earlier[28]. The inorganic phosphate was detected with Malachite Green reagent (0.005 % Carbinol hydrochloride, 1.7 % sulfuric acid, 0.14 % ammonium molybdate, 0.025 % Triton-X) at an absorbance of 620 nm.

Minimum inhibitory concentration (MIC_{90})

Mycobacterium bovis bacillus Calmette-Guerin (BCG) Montreal containing the pSMT1-*luxAB* plasmid was prepared as previously described[71]. Briefly, the mycobacteria were grown in Middlebrook 7H9 broth, supplemented with 10% ADC enrichment (Middlebrook Albumin Dextrose Catalase Supplement, Becton Dickinson, Oxford, UK) and hygromycin (50 mg/l; Roche, Lewes, UK), the culture was washed twice with sterile PBS, and re-suspended in broth and then dispensed into vials. Glycerol was added to a final concentration of 25% and the vials were frozen at −80°C. Prior to each experiment, a vial was defrosted, added to 9 mL of 7H9/ADC/hygromycin medium, and incubated with shaking for 72 h at 37°C. Mycobacteria were then centrifuged for 10 minutes at 3000×g, washed twice with PBS, and re-suspended in 10 ml of PBS. Resazurin microtiter assay (REMA) was used to determine the minimum inhibitory concentration (MIC_{90}) for the inhibitors against the mycobacterial strain. The inhibitors (10 μL) were added to bacterial suspensions (90 μL) on a 96-well plate at a concentration range between 0.4-50.0 μM. MIC was determined by the color change using resazurin (1:10 v/v, PrestoBlue Cell

516   viability reagent, Thermo Scientific). MIC was determined after one week by adding

517   10 μL resazurin followed by incubation overnight, corresponding to 90% inhibition.

518   *Human cytotoxicity assays*

519   Human venous blood mononuclear cells were obtained from healthy volunteers using

520   a Lymphoprep density gradient (Axis-Shield, Oslo, Norway) according to the

521   manufacturer's instructions. To obtain pure monocytes, CD14 micro beads were

522   applied to the cell suspension, washed and passed through a LS-column according to

523   manufacturer's description (130-050-201, 130-042-401, Miltenyi Biotec, USA). The

524   monocytes were counted (Sysmex), diluted in RPMI 1640 supplemented with 5%

525   FCS, NEAA, 1 mM Sodium Pyruvate, 0.1 mg/mL Gentamicin (11140-035, 111360-

526   039, 15710-49, Gibco, Life Technologies) and 50 ng/mL GM-CSF (215-GM, R&D

527   systems) and seeded in 96-well plates (10^5/well) for a week to differentiate into

528   macrophages. Infection experiments were performed in RPMI 1640 without

529   Gentamicin. The medium was replaced with fresh medium containing 6.3, 12.5, 25 or

530   50 μM inhibitor or DMSO and incubated 24 h in 5% CO_2 atmosphere. For

531   cytotoxicity   measurement,   10   μL   3-(4,5-dimethylthiazol-2-yl)-2,5

532   diphenyltetrazolium bromide (MTT) solution (Sigma) was added to each well

533   according to manufacturer's instructions and analysed in a spectrophotometer at 580

534   nm. NZX cytotoxicity was further examined by ATPlite™ assays. Primary

535   macrophages were treated with 6.3, 12.5, 25 or 50 μM inhibitor or DMSO (Sigma) for

536   24 hours. Cell viability was assessed with cellular ATP levels using ATPlite™ kit

537   (6016943, Perkin Elmer) compared to untreated controls, according to the

538   manufacturer's instructions.

539

540   *MD simulation*

541   The two crystal structures, E2-AlF$_4^-$ and E2-BeF$_3^-$, were inserted into a DOPC (1,2-

542   dioleoyl-sn-glycero-3-phosphocholine) membrane patch using the CHARMM-GUI

543   membrane builder[72]. The membrane positions were predicted by the Orientations of

544   Proteins in Membranes (OPM) server[73]. During the simulation equilibration phase,

545   position restraints were gradually released from the water and lipids for a total of 30

546   ns followed by 500 ns non-restrained production runs. Each protein state was

547   simulated in independent repeat simulations starting from a different set of initial

548   velocities, adding up to a sampling total of 500 ns x 4. A Nose-Hoover temperature

coupling[74] was applied using a reference temperature of 310 K. A Parrinello-Rahman pressure coupling[75] was applied with a reference pressure of 1 bar and compressibility of 4.5e-5 bar^{-1} in a semi-isotropic environment. The TIP3P water model was used and the system contained 0.15 M NaCl. The E2-AlF$_4^-$ system was composed of 256 lipids and 29,429 water molecules while E2-BeF$_3^-$ system was composed of 254 lipids and 30,535 water molecules. The systems were equilibrated and simulated using the GROMACS-2021 simulation package[76] and CHARMM36 all-atom force fields[77] for the protein and lipids. The membrane domain was used as alignment reference for the root means square deviation and center-of-mass calculations, and the protein backbone was used as alignment reference for calculating the root mean square fluctuation. The secondary structure was assessed with the do_dssp tool in GROMACS-2021[76].

591

592   **Data Information**

593   Atomic coordinates and structure factors for the sCoaT AlF_4^-- and BeF_3^--stabilized

594   crystal structures have been deposited at the Protein Data Bank (PDB) under

595   accession codes 7QBZ and 7QC0. The authors declare no competing financial

596   interests. Correspondence and requests for materials should be addressed to P.G.

597   (pontus@sund.ku.dk).
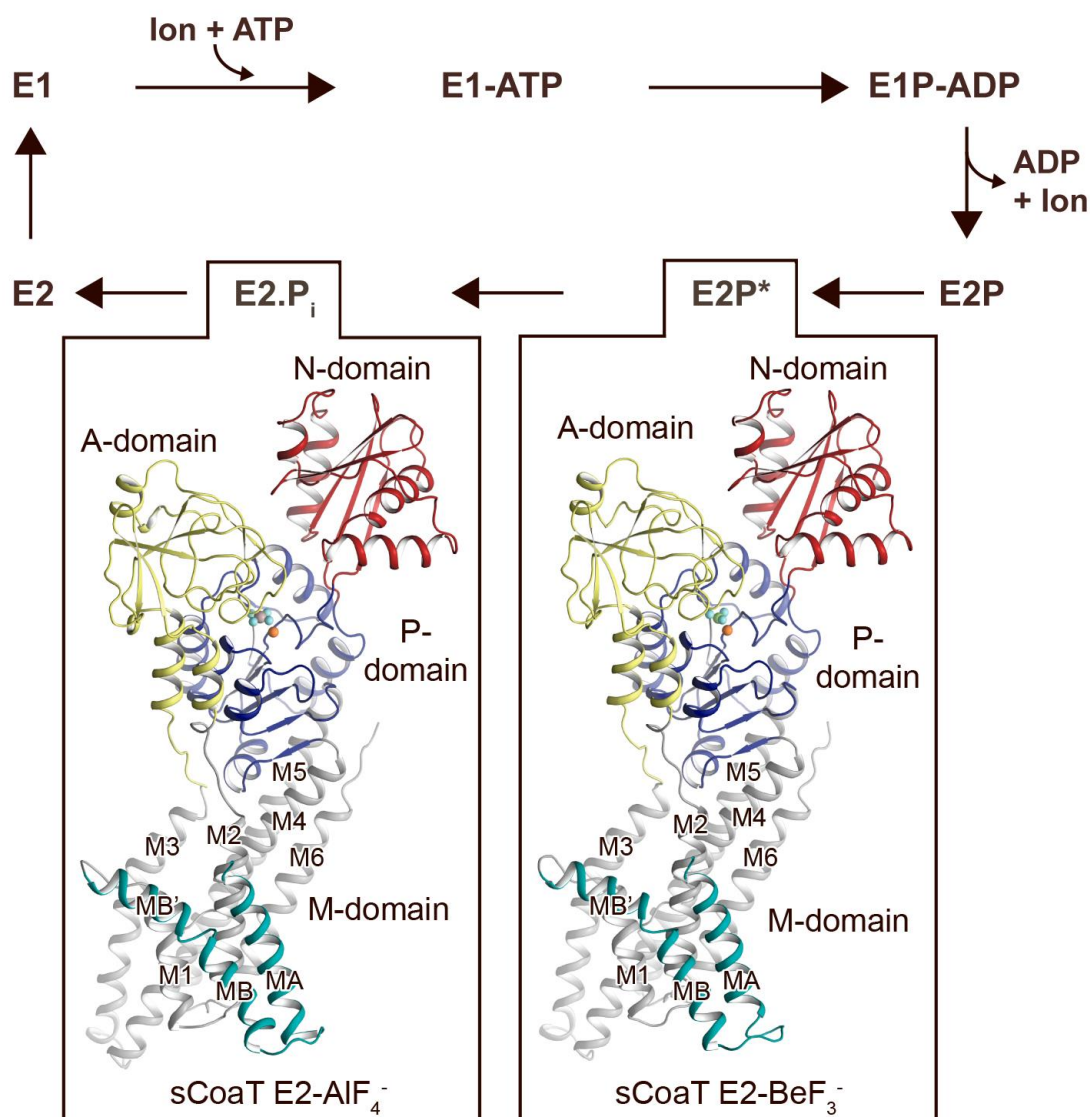
Figures

Figure 1 │Overall architecture and reaction cycle. The sCoaT structures reveal that P_{IB-4}-ATPases comprise soluble A-, P- and N-domains, shown in yellow, blue and red, respectively, as well as a transmembrane domain with eight helices: MA and MB, in cyan, and M1-M6, in grey, and that the P_{IB-4}-topology lacks classical so-called heavy metal binding domain. The transport mechanism of P-type ATPases depends on ATP-dependent phosphorylation and auto-dephosphorylation, and include four principal conformations, E1, E1P, E2P and E2, where P denote phosphorylation. The determined structures are trapped in two transition states following ion-release – an occluded late E2P (E2P*) and an occluded transition state of dephosphorylation, E2.P$_{i.}$
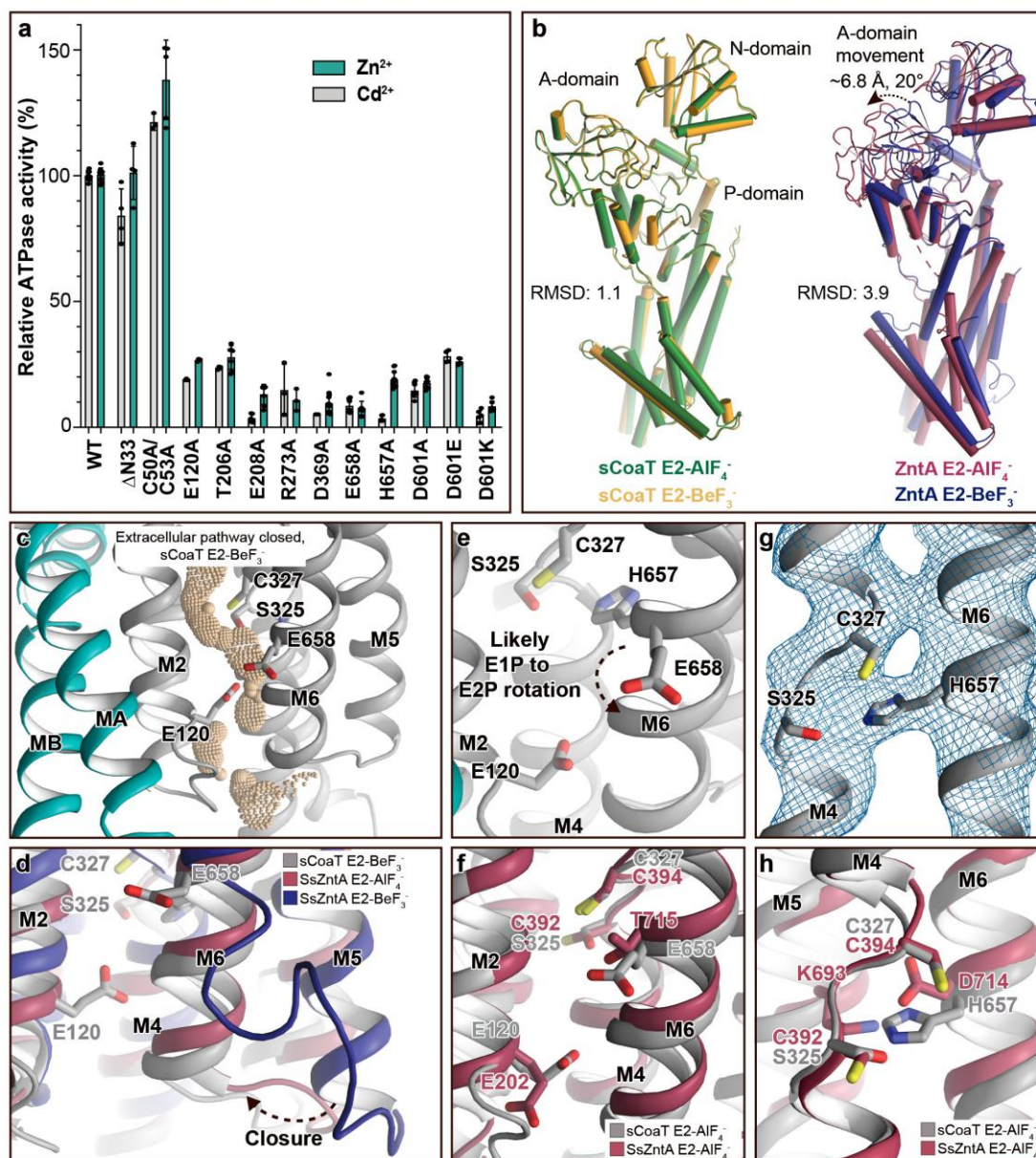
Figure 2 │ Mechanistic insight into the function of P$_{IB-4}$-ATPases. a, Functional ATPase assay in lipid-detergent solution with targeted residues in sequential order. The wild-type (WT) specific activity using the employed experimental conditions in the presence of 50 μM metal is 1.00 ± 0.01 μmol mg^{-1} min^{-1} with Zn^{2+} and 2.80 ± 0.06 μmol mg^{-1} min^{-1} with Cd^{2+}, comparable to the activity previously measured for P$_{IB-4}$-ATPases. For biological averages and s.d. see **Figure 2 – figure supplement 1e**. **b,** Comparisons of E2-AlF$_4^-$ and E2-BeF$_3^-$ structures of sCoaT and the equivalent of SsZntA (PDB ID of SsZntA structures: 4UMV and 4UMW). All superimpositions were performed based on the P-domain, and the RMSD values for the overall structures are indicated. **c,** Identified cavity (wheat) in the E2-BeF$_3^-$ structure using the software HOLE. The E2-BeF$_3^-$ and the E2-AlF$_4^-$ (not shown) structure are

occluded, lacking continuous connection between the ion-binding site to the outward environment. **d,** The conformational changes that likely allow for closure of the release pathway, as illustrated from the E2-BeF$_3^-$ structure of SsZntA to the E2-AlF$_4^-$ structures of sCoaT or SsZntA. **e-h,** Close-views of ion-binding and -release residues in the M-domain of sCoaT and SsZntA. **e,** The orientation of E658 is incompatible with high-affinity binding, and is likely contributing to ion-release. **f,** Release likely takes place via E658 and E120. **g,** The sandwiched position between S325 and C327 of H657, including the final 2Fo-Fc electron density (blue). **h,** The position of H657 in sCoaT overlaps with the one of K693 in SsZntA, and both likely serve as in-built counter-ions.
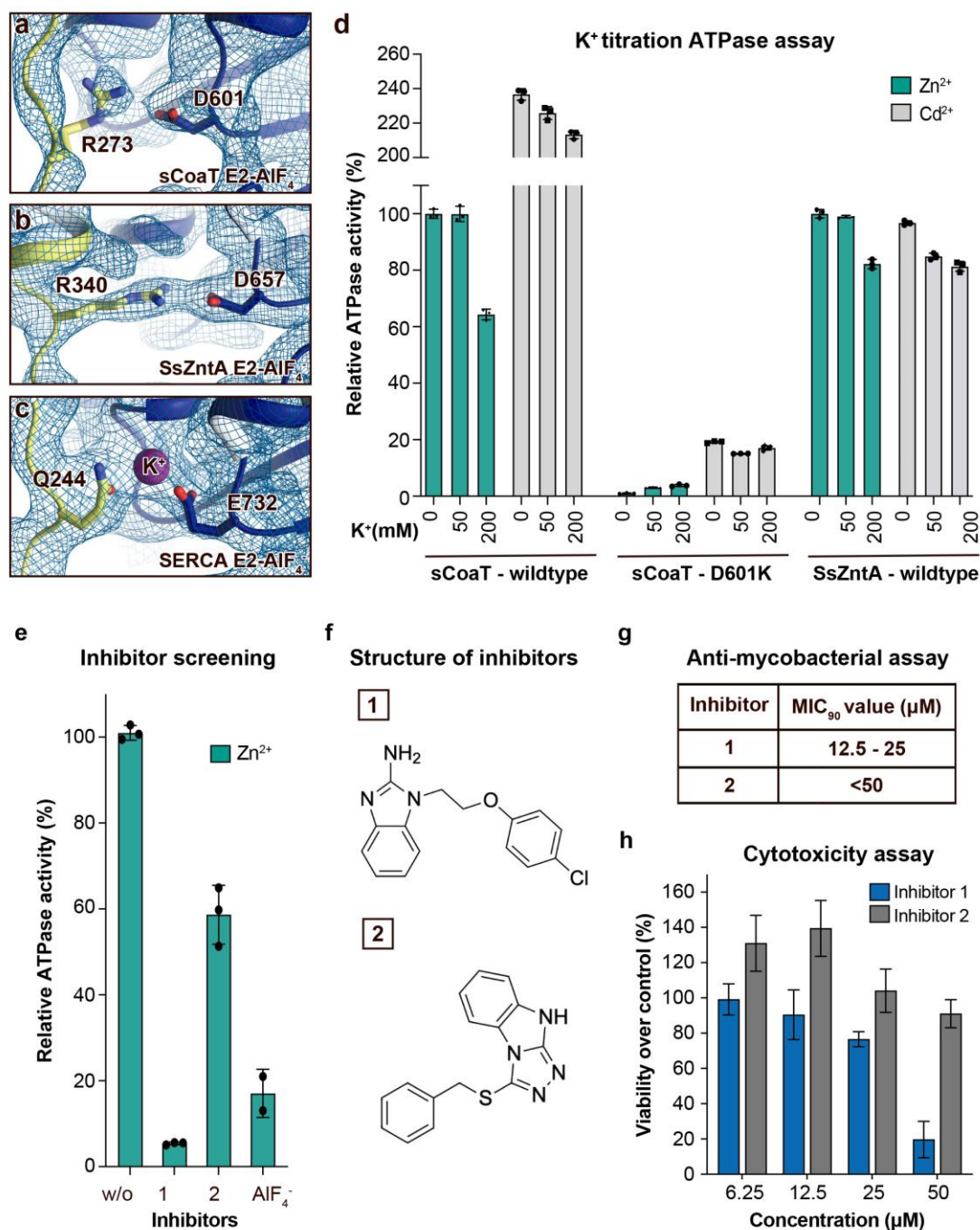
Figure 3│Regulation and inhibition. a-c, Close-views of the regulatory point of interaction between the A- and P-domains in the E2-AlF$_4^-$ structures of sCoaT, SsZntA and SERCA (PDB IDs 4UMW and 1XP5) with the corresponding 2Fo-Fc electron density shown at σ=1.0 (blue mesh). **a,** sCoaT (colored as in Figure 1) with interaction between D601 and R273. **b,** SsZntA (shown as panel a) with interaction between D657 and R340. **c,** SERCA (shown as in panel a) with bound K$^+$ (purple) between E732 and Q244. **d,** Functional ATPase assay in lipid-detergent solution of sCoaT (wild-type and D601K forms) as well as SsZntA (wild-type), using protein

641   samples purified in the absence of K^+ and Na^+ (see Methods). The mean + s.d. of

642   technical replicates is shown (n=3). KCl leaves the function of sCoat and SsZntA

643   essentially unaffected in the presence of Zn^{2+} (cyan) or Cd^{2+} (gray). The equivalent

644   form of sCoaT D601K has previously been exploited to demonstrate K^+-dependence

645   in the Na,K-ATPase [56]. Collectively, these data suggest that the P-/A-domain site

646   regulation is K^+-independent in P_{IB}-ATPases, in contrast to classical P-type ATPases.

647   **e-h** Evaluation of the effect on selected identified novel inhibitors on activity of

648   protein, as well as survival of mycobacteria and primary human macrophages. **e,**

649   Effect of two inhibitors (300 μM) on the activity of sCoaT assessed in lipid-detergent

650   solution in the presence of Zn^{2+}. For comparison, the commonly used P-type ATPase

651   inhibitor AlF_4^- (500 μM) is included. **f,** The structure of inhibitor 1 and 2. **g,** The

652   minimal inhibitory concentration to kill 90 % (MIC_{90}) of mycobacteria for inhibitor 1

653   and 2. The mean MIC_{90} value for inhibitor 1 is 18.75 μM, while for inhibitor 2 it is

654   over 50 μM. The values are based on four separate experiments. **h,** The cytotoxic

655   effect of different concentrations of inhibitor 1 and 2 on primary human macrophages

656   (ATP assay). The standard error of mean (SEM) of 9 replicates is shown (n=9).

657
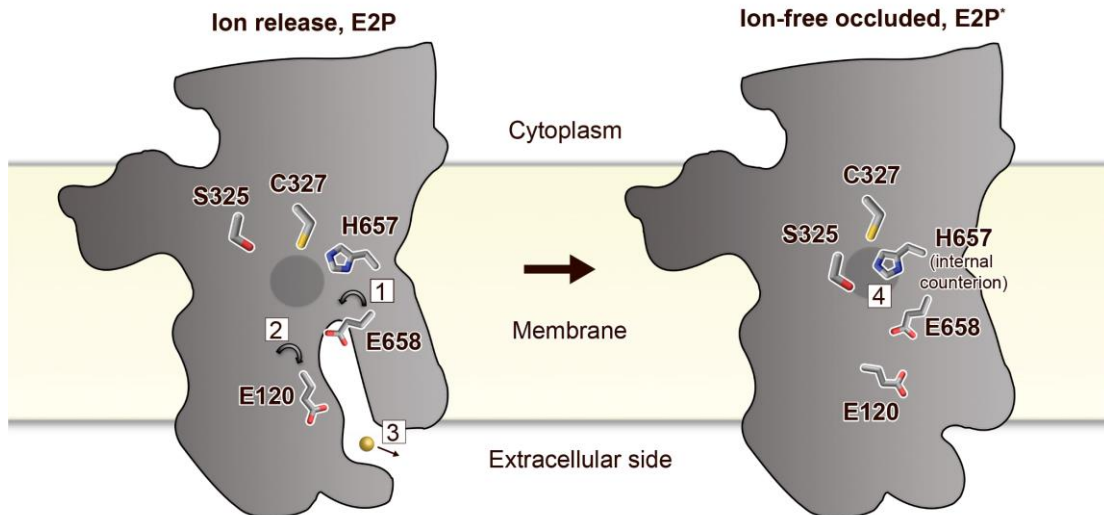
Figure 4│Putative ion-release and re-occlusion mechanism of P$_{IB-4}$-ATPases.
Schematic model illustrating the transmembrane domain (the soluble domains have
been removed for clarity) of two separate states, an E2P and an occluded E2P*
conformation as the determined structure (E2-BeF$_3^-$), respectively. Zinc or cadmium
release from the high affinity binding site in the M-domain is likely permitted through
re-orientation of E658 (1) in the E1P to E2P transition, thereby lowering the affinity
for the occluded ion. E120 serves as a transient linker between the high-affinity
binding site and the outward environment (2). Following ion-release (3) H657 shifts
to a sandwiched position between S325 and C327 (4), acting as a built-in counter ion,
preventing back-transfer of the released ion, and allowing completion of the reaction
cycle.

	E2-BeF$_3^-$	E2-AlF$_4^-$
Data collection		
Wavelength (Å)	1.0	1.0
Space group	P 21 21 2	P 21 21 2
Cell dimensions		
a, b, c (Å)	89.0 94.5 128.8	89.6 93.7 128.3
α, β, γ (°)	90 90 90	90 90 90
Resolution (Å)	47.3-3.1	45.6-3.3
	(3.22-3.11)	(3.37-3.25)
R_{merge}(%)	11.4 (276.3)	15.5 (246)
$I / \sigma I$	17.8 (1.12)	8.5 (0.98)
CC$_{1/2}$	1 (0.475)	0.99 (0.37)
Completeness (%)	97.3 (99.8)	99.2 (99.9)
Redundancy	13.3 (13.8)	6.1 (6.6)
Refinement		
Resolution (Å)	47.3-3.1	45.6-3.3
	(3.22-3.11)	(3.37-3.25)
No. reflections	19643 (1963)	17466 (1714)
R_{work} / R_{free} (%)	24.4/26.8	21.8/25.5
No. of atoms		
Protein	4695	4695
Ligand/ion	5	6
Water	10	0
Average B-factors		
Protein	135.91	152.54
Ligand/ion	84.15	86.47
Solvent	79.62	
R.m.s. deviations		
Bond lengths (Å)	0.004	0.003
Bond angles (°)	0.77	0.83
Ramachandran statistics		
Favored (%)	97.8	96.9
Allowed (%)	2.2	3.1
Outliers (%)	0.0	0.0
Clashscore	1.05	7.89
MolProbity score	0.85	1.62

669 **Table 1 ⎢ Data collection and refinement statistics.** Statistics for the highest

670 resolution shell are shown in parentheses.

671 **References**

672 1. K. J. Waldron, J. C. Rutherford, D. Ford, N. J. Robinson, Metalloproteins and
673 metal sensing. *Nature* **460**, 823-830 (2009).

674 2. H. Kozlowski *et al.*, Copper, iron, and zinc ions homeostasis and their role
675 in neurodegenerative disorders (metal uptake, transport, distribution and
676 regulation). *Coordin Chem Rev* **253**, 2665-2685 (2009).

677 3. P. C. Bull, G. R. Thomas, J. M. Rommens, J. R. Forbes, D. W. Cox, The Wilson
678 Disease Gene Is a Putative Copper Transporting P-Type Atpase Similar to
679 the Menkes Gene. *Nature Genetics* **5**, 327-337 (1993).

680 4. C. Vulpe, B. Levinson, S. Whitney, S. Packman, J. Gitschier, Isolation of a
681 candidate gene for Menkes disease and evidence that it encodes a copper-
682 transporting ATPase. *Nat Genet* **3**, 7-13 (1993).

683 5. R. W. Albers, S. Fahn, G. J. Koval, The Role of Sodium Ions in the Activation
684 of Electrophorus Electric Organ Adenosine Triphosphatase. *Proceedings of*
685 *the National Academy of Sciences of the United States of America* **50**, 474-
686 481 (1963).

687 6. R. L. Post, A. K. Sen, An Enzymatic Mechanism of Active Sodium and
688 Potassium Transport. *J Histochem Cytochem* **13**, 105-112 (1965).

689 7. C. Toyoshima, M. Nakasako, H. Nomura, H. Ogawa, Crystal structure of the
690 calcium pump of sarcoplasmic reticulum at 2.6 A resolution. *Nature* **405**,
691 647-655 (2000).

692 8. C. Toyoshima, H. Nomura, Structural changes in the calcium pump
693 accompanying the dissociation of calcium. *Nature* **418**, 605-611 (2002).

694 9. C. Toyoshima, H. Nomura, T. Tsuda, Lumenal gating mechanism revealed
695 in calcium pump crystal structures with phosphate analogues. *Nature*
696 **432**, 361-368 (2004).

697 10. C. Olesen, T. L. Sorensen, R. C. Nielsen, J. V. Moller, P. Nissen,
698 Dephosphorylation of the calcium pump coupled to counterion occlusion.
699 *Science* **306**, 2251-2255 (2004).

700 11. C. Olesen *et al.*, The structural basis of calcium transport by the calcium
701 pump. *Nature* **450**, 1036-1042 (2007).

702 12. A. M. Winther *et al.*, The sarcolipin-bound calcium pump stabilizes
703 calcium sites exposed to the cytoplasm. *Nature* **495**, 265-269 (2013).

704 13. C. Toyoshima *et al.*, Crystal structures of the calcium pump and sarcolipin
705 in the Mg2+-bound E1 state. *Nature* **495**, 260-264 (2013).

706 14. J. P. Morth *et al.*, Crystal structure of the sodium-potassium pump. *Nature*
707 **450**, 1043-1049 (2007).

708 15. T. Shinoda, H. Ogawa, F. Cornelius, C. Toyoshima, Crystal structure of the
709 sodium-potassium pump at 2.4 A resolution. *Nature* **459**, 446-450 (2009).

710 16. A. T. Smith, K. P. Smith, A. C. Rosenzweig, Diversity of the metal-
711 transporting P1B-type ATPases. *J Biol Inorg Chem* **19**, 947-960 (2014).

712 17. J. M. Arguello, Identification of ion-selectivity determinants in heavy-
713 metal transport P1B-type ATPases. *J Membr Biol* **195**, 93-108 (2003).

714 18. E. L. Zielazinski, G. E. Cutsail, 3rd, B. M. Hoffman, T. L. Stemmler, A. C.
715 Rosenzweig, Characterization of a cobalt-specific P(1B)-ATPase.
716 *Biochemistry* **51**, 7891-7900 (2012).

717 19. D. Zhitnitsky, O. Lewinson, Identification of functionally important
718 conserved trans-membrane residues of bacterial PIB -type ATPases. *Mol*
719 *Microbiol* **91**, 777-789 (2014).

720 20. C. M. Sassetti, E. J. Rubin, Genetic requirements for mycobacterial survival
721   during infection. *Proceedings of the National Academy of Sciences of the*
722   *United States of America* **100**, 12989-12994 (2003).
723 21. S. M. Joshi *et al.*, Characterization of mycobacterial virulence genes
724   through genetic interaction mapping. *Proceedings of the National Academy*
725   *of Sciences of the United States of America* **103**, 11760-11765 (2006).
726 22. D. Raimunda, J. E. Long, C. M. Sassetti, J. M. Arguello, Role in metal
727   homeostasis of CtpD, a Co(2)(+) transporting P(1B4)-ATPase of
728   Mycobacterium smegmatis. *Mol Microbiol* **84**, 1139-1149 (2012).
729 23. I. Moreno *et al.*, AtHMA1 is a thapsigargin-sensitive Ca2+/heavy metal
730   pump. *Journal of Biological Chemistry* **283**, 9633-9641 (2008).
731 24. J. Scherer, D. H. Nies, CzcP is a novel efflux system contributing to
732   transition metal resistance in Cupriavidus metallidurans CH34. *Mol*
733   *Microbiol* **73**, 601-621 (2009).
734 25. D. Seigneurin-Berny *et al.*, HMA1, a new Cu-ATPase of the chloroplast
735   envelope, is essential for growth under adverse light conditions. *Journal of*
736   *Biological Chemistry* **281**, 2882-2892 (2006).
737 26. A. T. Smith, M. O. Ross, B. M. Hoffman, A. C. Rosenzweig, Metal Selectivity
738   of a Cd-, Co-, and Zn-Transporting P1B-type ATPase. *Biochemistry* **56**, 85-
739   95 (2017).
740 27. P. Gourdon *et al.*, Crystal structure of a copper-transporting PIB-type
741   ATPase. *Nature* **475**, 59-U74 (2011).
742 28. K. Wang *et al.*, Structure and mechanism of Zn2+-transporting P-type
743   ATPases. *Nature* **514**, 518-522 (2014).
744 29. M. Andersson *et al.*, Copper-transporting P-type ATPases use a unique
745   ion-release pathway. *Nat Struct Mol Biol* **21**, 43-+ (2014).
746 30. A. C. Rosenzweig, J. M. Arguello, Toward a molecular understanding of
747   metal transport by P(1B)-type ATPases. *Curr Top Membr* **69**, 113-136
748   (2012).
749 31. S. L. Drees, D. F. Beyer, C. Lenders-Lomscher, M. Lubben, Distinct
750   functions of serial metal-binding domains in the Escherichia coliP(1B)-
751   ATPase CopA. *Molecular Microbiology* **97**, 423-438 (2015).
752 32. M. Gonzalez-Guerrero, J. M. Arguello, Mechanism of Cu+-transporting
753   ATPases: soluble Cu+ chaperones directly transfer Cu+ to transmembrane
754   transport sites. *Proceedings of the National Academy of Sciences of the*
755   *United States of America* **105**, 5992-5997 (2008).
756 33. D. Mattle *et al.*, On allosteric modulation of P-type Cu(+)-ATPases. *J Mol*
757   *Biol* **425**, 2299-2308 (2013).
758 34. O. Sitsel *et al.*, Structure and Function of Cu(I)- and Zn(II)-ATPases.
759   *Biochemistry* **54**, 5673-5683 (2015).
760 35. P. A. Lanzetta, L. J. Alvarez, P. S. Reinach, O. A. Candia, An improved assay
761   for nanomole amounts of inorganic phosphate. *Anal Biochem* **100**, 95-97
762   (1979).
763 36. D. Osman *et al.*, Bacterial sensors define intracellular free energies for
764   correct enzyme metalation. *Nat Chem Biol* **15**, 241-249 (2019).
765 37. P. Gourdon *et al.*, Crystal structure of a copper-transporting PIB-type
766   ATPase. *Nature* **475**, 59-64 (2011).

767   38.   M. Andersson *et al.*, Copper-transporting P-type ATPases use a unique
768   ion-release pathway. *Nature structural & molecular biology* **21**, 43-48
769   (2014).
770   39.   P. Gourdon *et al.*, HiLiDe-Systematic Approach to Membrane Protein
771   Crystallization in Lipid and Detergent. *Cryst Growth Des* **11**, 2098-2106
772   (2011).
773   40.   T. L. Sorensen, C. Olesen, A. M. Jensen, J. V. Moller, P. Nissen, Crystals of
774   sarcoplasmic reticulum Ca(2+)-ATPase. *J Biotechnol* **124**, 704-716 (2006).
775   41.   T. Croll, ISOLDE: a physically realistic environment for model building
776   into low-resolution electron-density maps. *Acta Crystallographica Section*
777   *D* **74**, 519-530 (2018).
778   42.   G. P. Borrelly, S. A. Rondet, S. Tottey, N. J. Robinson, Chimeras of P-type
779   ATPases and their transcriptional regulators: contributions of a cytosolic
780   amino-terminal domain to metal specificity. *Mol Microbiol* **53**, 217-227
781   (2004).
782   43.   C. H. Yu *et al.*, The metal chaperone Atox1 regulates the activity of the
783   human copper transporter ATP7B by modulating domain dynamics. *J Biol*
784   *Chem* **292**, 18169-18177 (2017).
785   44.   I. Morin, S. Gudin, E. Mintz, M. Cuillel, Dissecting the role of the N-terminal
786   metal-binding domains in activating the yeast copper ATPase in vivo. *Febs*
787   *Journal* **276**, 4483-4495 (2009).
788   45.   D. Mattle *et al.*, A sulfur-based transport pathway in Cu+-ATPases. *EMBO*
789   *Rep* **16**, 728-740 (2015).
790   46.   S. B. Hansen *et al.*, The crystal structure of the Ca^{2+}-ATPase
791   1 from Listeria monocytogenes reveals a pump primed for
792   dephosphorylation. *bioRxiv*, 2020.2006.2023.166462 (2020).
793   47.   S. J. Patel *et al.*, Fine-tuning of Substrate Affinity Leads to Alternative
794   Roles of Mycobacterium tuberculosis Fe2+-ATPases. *J Biol Chem* **291**,
795   11529-11539 (2016).
796   48.   J. V. Moller, C. Olesen, A. M. Winther, P. Nissen, The sarcoplasmic Ca2+-
797   ATPase: design of a perfect chemi-osmotic pump. *Q Rev Biophys* **43**, 501-
798   566 (2010).
799   49.   K. Faxen *et al.*, Characterization of a Listeria monocytogenes Ca(2+)
800   pump: a SERCA-type ATPase with only one Ca(2+)-binding site. *J Biol*
801   *Chem* **286**, 1609-1617 (2011).
802   50.   K. Abe, K. Irie, H. Nakanishi, H. Suzuki, Y. Fujiyoshi, Crystal structures of
803   the gastric proton pump. *Nature* **556**, 214-218 (2018).
804   51.   M. Dyla, M. Kjaergaard, H. Poulsen, P. Nissen, Structure and Mechanism of
805   P-Type ATPase Ion Pumps. *Annu Rev Biochem* **89**, 583-603 (2020).
806   52.   B. P. Pedersen, M. J. Buch-Pedersen, J. P. Morth, M. G. Palmgren, P. Nissen,
807   Crystal structure of the plasma membrane proton pump. *Nature* **450**,
808   1111-1114 (2007).
809   53.   H. Nakanishi *et al.*, Transport Cycle of Plasma Membrane Flippase ATP11C
810   by Cryo-EM. *Cell Rep* **32**, 108208 (2020).
811   54.   N. Abeyrathna, S. Abeyrathna, M. T. Morgan, C. J. Fahrni, G. Meloni,
812   Transmembrane Cu(i) P-type ATPase pumps are electrogenic uniporters.
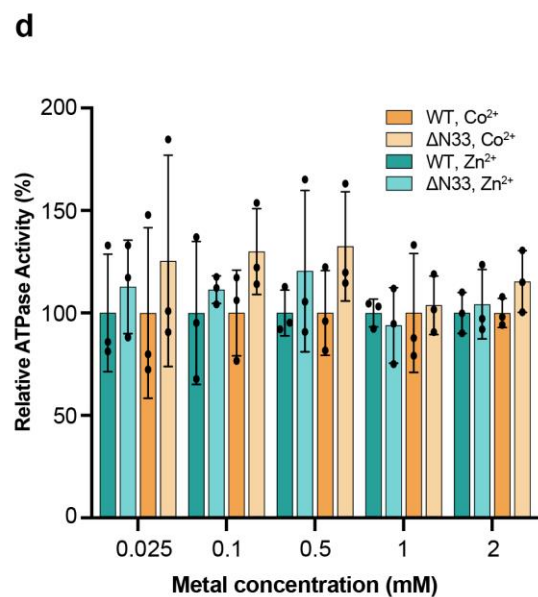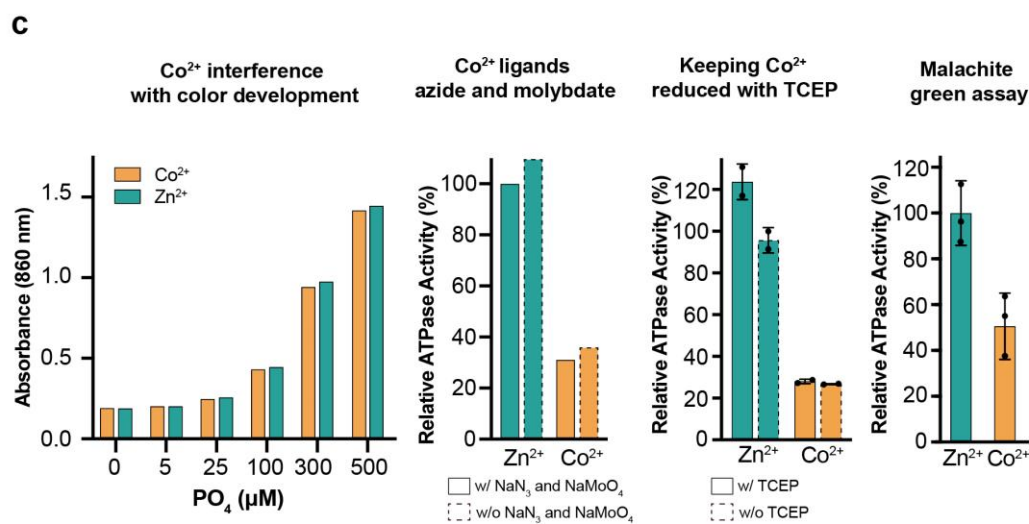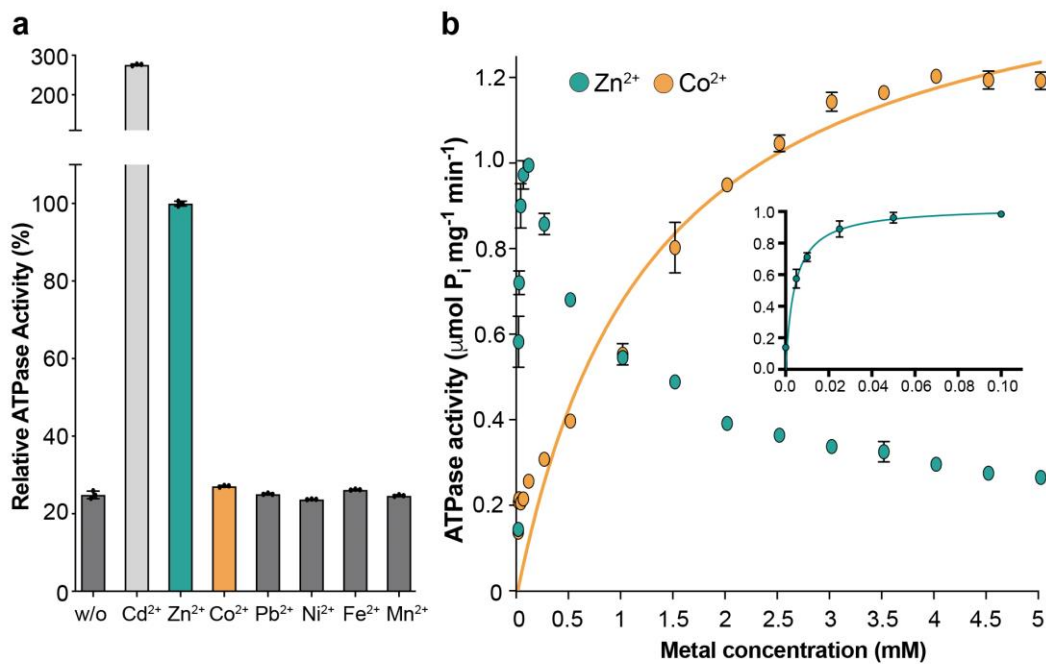813   *Dalton Trans*, (2020).

814 55. T. L.-M. Sørensen *et al.*, Localization of a K+-binding Site Involved in
815   Dephosphorylation of the Sarcoplasmic Reticulum Ca2+-ATPase. *Journal*
816   *of Biological Chemistry* **279**, 46355-46358 (2004).
817 56. V. R. Schack *et al.*, Identification and function of a cytoplasmic K+ site of
818   the Na+, K+ -ATPase. *J Biol Chem* **283**, 27982-27990 (2008).
819 57. C. M. Sassetti, E. J. Rubin, Genetic requirements for mycobacterial survival
820   during infection. *Proc Natl Acad Sci U S A* **100**, 12989-12994 (2003).
821 58. S. M. Joshi *et al.*, Characterization of mycobacterial virulence genes
822   through genetic interaction mapping. *Proc Natl Acad Sci U S A* **103**,
823   11760-11765 (2006).
824 59. H. Botella *et al.*, Mycobacterial p(1)-type ATPases mediate resistance to
825   zinc poisoning in human macrophages. *Cell Host Microbe* **10**, 248-259
826   (2011).
827 60. H. Pi, S. J. Patel, J. M. Arguello, J. D. Helmann, The Listeria monocytogenes
828   Fur-regulated virulence protein FrvA is an Fe(II) efflux P1B4 -type
829   ATPase. *Mol Microbiol* **100**, 1066-1079 (2016).
830 61. M. M. Bradford, Rapid and Sensitive Method for Quantitation of
831   Microgram Quantities of Protein Utilizing Principle of Protein-Dye
832   Binding. *Anal Biochem* **72**, 248-254 (1976).
833 62. A. J. McCoy *et al.*, Phaser crystallographic software. *Journal of applied*
834   *crystallography* **40**, 658-674 (2007).
835 63. D. Liebschner *et al.*, Macromolecular structure determination using X-
836   rays, neutrons and electrons: recent developments in Phenix. *Acta*
837   *Crystallographica Section D* **75**, 861-877 (2019).
838 64. P. Emsley, B. Lohkamp, W. G. Scott, K. Cowtan, Features and development
839   of Coot. *Acta Crystallographica Section D* **66**, 486-501 (2010).
840 65. T. I. Croll, ISOLDE: a physically realistic environment for model building
841   into low-resolution electron-density maps. *Acta Crystallogr D* **74**, 519-530
842   (2018).
843 66. T. D. Goddard *et al.*, UCSF ChimeraX: Meeting modern challenges in
844   visualization and analysis. *Protein Sci* **27**, 14-25 (2018).
845 67. P. V. Afonine *et al.*, Towards automated crystallographic structure
846   refinement with phenix.refine. *Acta Crystallographica Section D* **68**, 352-
847   367 (2012).
848 68. C. J. Williams *et al.*, MolProbity: More and better reference data for
849   improved all-atom structure validation. *Protein Sci* **27**, 293-315 (2018).
850 69. W. L. DeLano, Pymol: An open-source molecular graphics tool. *CCP4*
851   *Newsletter on protein crystallography* **40**, 82-92 (2002).
852 70. E. S. Baginski, P. P. Foa, B. Zak, Microdetermination of inorganic
853   phosphate, phospholipids, and total phosphate in biologic materials. *Clin*
854   *Chem* **13**, 326-332 (1967).
855 71. V. A. Snewin *et al.*, Assessment of immunity to mycobacterial infection
856   with luciferase reporter constructs. *Infect Immun* **67**, 4586-4593 (1999).
857 72. E. L. Wu *et al.*, CHARMM-GUI Membrane Builder toward realistic
858   biological membrane simulations. *J Comput Chem* **35**, 1997-2004 (2014).
859 73. M. A. Lomize, I. D. Pogozheva, H. Joo, H. I. Mosberg, A. L. Lomize, OPM
860   database and PPM web server: resources for positioning of proteins in
861   membranes. *Nucleic Acids Res* **40**, D370-376 (2012).

862 74. S. Nosé, M. Klein, Constant pressure molecular dynamics for molecular
863   systems. *Molecular Physics* **50**, 1055-1076 (1983).
864 75. M. Parrinello, A. Rahman, Polymorphic transitions in single crystals: A
865   new molecular dynamics method. *Journal of Applied physics* **52**, 7182-
866   7190 (1981).
867 76. M. J. Abraham *et al.*, GROMACS: High performance molecular simulations
868   through multi-level parallelism from laptops to supercomputers.
869   *SoftwareX* **1**, 19-25 (2015).
870 77. R. B. Best *et al.*, Optimization of the additive CHARMM all-atom protein
871   force field targeting improved sampling of the backbone phi, psi and side-
872   chain chi(1) and chi(2) dihedral angles. *J Chem Theory Comput* **8**, 3257-
873   3273 (2012).
874 78. B. Mitra, R. Sharma, The cysteine-rich amino-terminal domain of ZntA, a
875   Pb(II)/Zn(II)/Cd(II)-translocating ATPase from Escherichia coli, is not
876   essential for its function. *Biochemistry* **40**, 7694-7699 (2001).
877
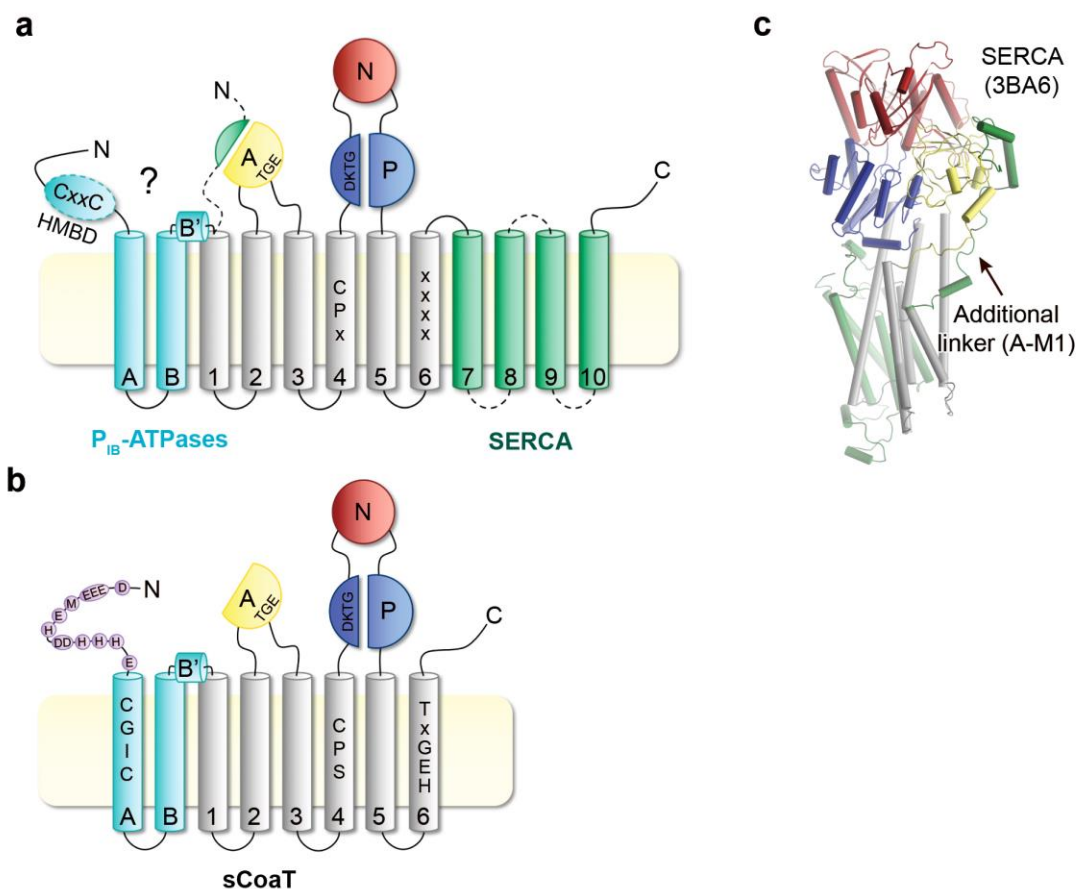
880

881 **Figure 1 – figure supplement 1 │ Topology comparison.** Topological differences
882 between P_{IB}-ATPases and classical P-type ATPases such as sCoaT and SERCA,
883 respectively. **a,** Schematic topology of P-type ATPases showing features unique to
884 P_{IB}-ATPases (the so-called heavy metal binding domain, HMBD, and transmembrane
885 helices MA-MB in cyan) and SERCA (an extended A-domain, an additional A-
886 domain linker and M7–M10 transmembrane helices in green). Location of key
887 residues in the M-domain for P_{IB}-ATPases are highlighted. **b,** The structure of
888 SERCA (PDB ID 3BA6), colored as the schematic topology highlighting the
889 additional linker to the A-domain. **c,** Topology of the P_{IB-4}-ATPase sCoaT. The
890 present work discloses the presence of helices MA, MB, MB' and that the core of P_{IB-}
891 $_4$-ATPases is devoid of classical HMBD, representing a previously elusive matter.
892 The cysteine pair (CGIC in the sequence) in the N-terminus of sCoaT is rather
893 positioned in MA. The N-terminus of sCoaT is rich in methionine, cysteine, histidine,
894 aspartate and glutamate residues (shown as purple circles), amino acids that can bind
895 metal.

897   **Figure 2 – figure supplement 1 │ Metal selectivity screening and reproducibility.**

898   **a,** Screen of different transition metals, tested at 50 μM each. There is clear metal-

899   dependent ATPase activity with Zn^{2+} (1.0 ± 0.01 μmol mg^{-1} min^{-1}) and Cd^{2+} (2.8 ±

900   0.05 μmol mg^{-1} min^{-1}), comparable to the activity previously measured for P_{IB-4}-

901   ATPases and also to Zn^{2+}-dependent activity of SsZntA (0.59±0.02 μmol mg^{-1} min^{-}

902   ^{1})[28]. In contrast, only low ATPase activity (about 5 % of the wild-type, corrected for

903   the background observed with no metal added) was detected with Co^{2+} for sCoaT. **b,**

904   Titration of zinc and cobalt. Co^{2+}-induced ATPase activity predominates above 1

905   mM, while at lower concentrations Zn^{2+} stimulates activity at a faster rate. The data

906   yield K_M values of 1.3 mM and 4.1 μM for Co^{2+} and Zn^{2+}, respectively. The

907   corresponding for the SsZntA related pump EcZntA is 10 μM with Zn^{2+} [78]. **c,**

908   Screening of assay conditions and assay type. **d,** The effect of the N-terminal tail on

909   the ion-specificity. Relative activity in the presence of Co^{2+} and Zn^{2+} (100 % is equal

910   to the activity measured for wild type at every measured metal type and

911   concentration), respectively, at five different metal concentrations, suggesting that the

912   tail is no major determinant for metal specificity. **e**, Biological and technical

913   replicates exploited to generate the error bars in **Figure 2a**.

914
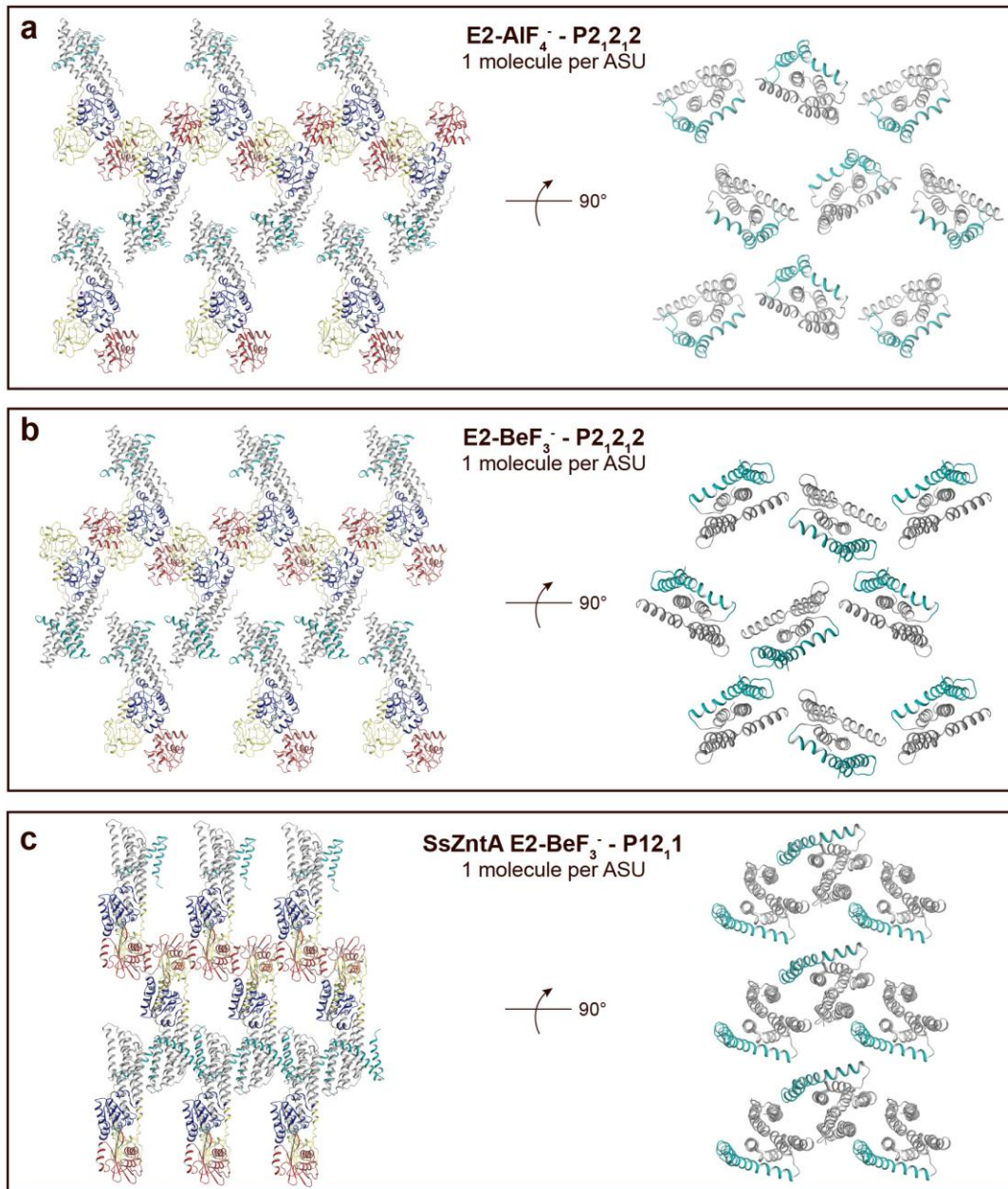
Figure 1 – figure supplement 2 │ Crystal packing of sCoaT E2-AlF$_4^-$ compared to the E2-BeF$_3^-$ crystal form of ZntA from *Shigella sonnei* (SsZntA, PDB ID: 4UMV). The domains are coloured as in Figure 1b. **a**, sCoaT E2-AlF$_4^-$ (P2$_1$2$_1$2, with 1 molecule per asymmetric unit). Left: View of the membrane layer. Right: 90° rotation view (compared to panel to the left) showing only the transmembrane domains. Equivalent views of the sCoaT E2-BeF$_3^-$ (P2$_1$2$_1$2) (**b**) and the SsZntA E2-BeF$_3^-$ (P12$_1$1) (**c**) crystal forms. Note the loose packing of the sCoaT crystals compared to that of SsZntA E2-BeF$_3^-$.

923
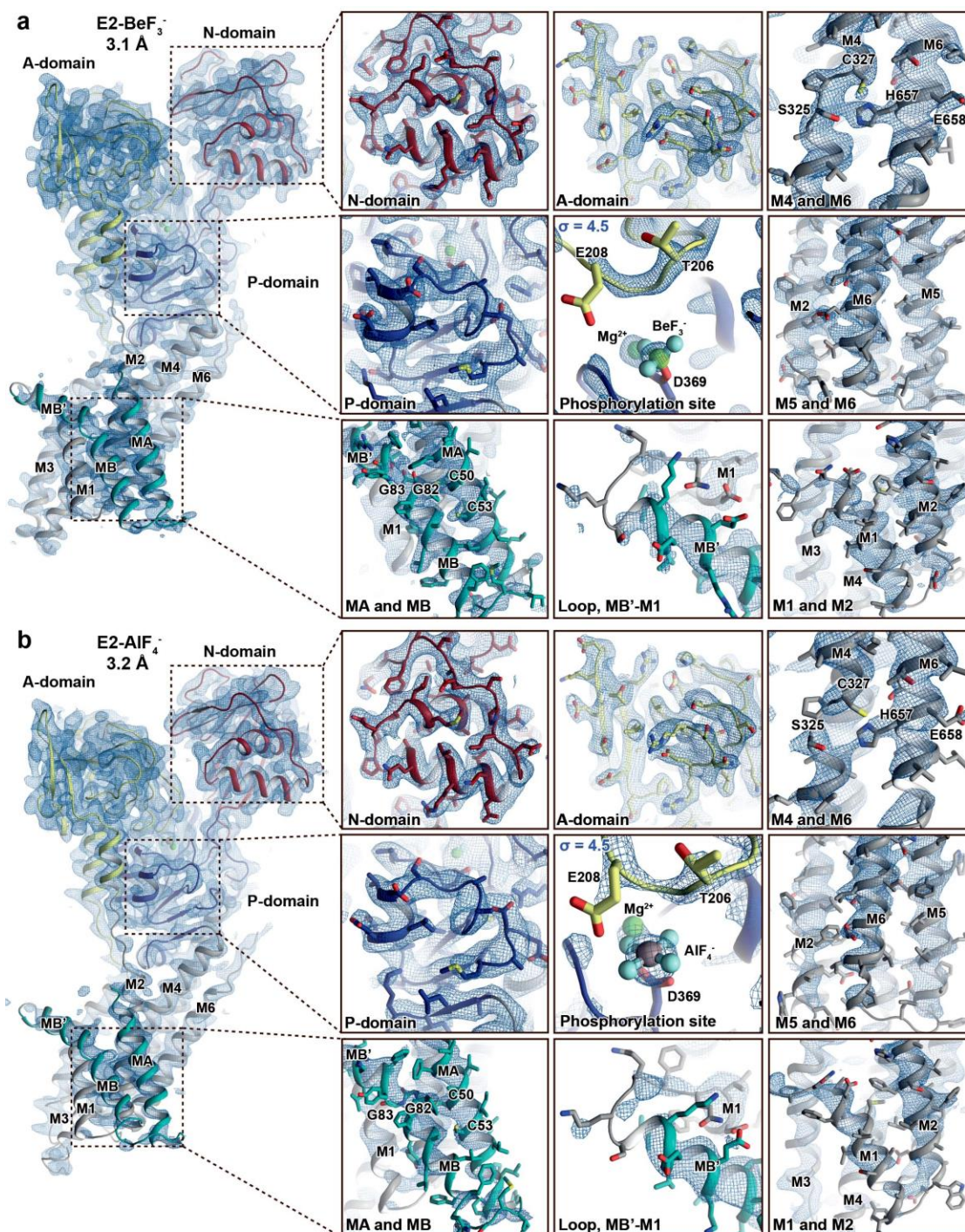
Figure 1 – figure supplement 3 │ Electron density quality. Final, sharpened, 2Fo-Fc electron density at σ=1.0 (blue mesh) if not otherwise stated. The overall resolution is indicated and the structures are colored as in Figure 1. **a,** E2-BeF$_3^-$ and **b,** E2-AlF$_4^-$. The quality of the maps differs between structures and domains. The A-, P- and N-domains are well-resolved in both structures. The M-domain is in general less well-resolved than the soluble domains, and the domain is somewhat more well-resolved in the E2-BeF$_3^-$ structure than in E2-AlF$_4^-$ structure. Nevertheless, it is still clear that MA and MB is present and that C50 and C53 in the N-terminus is

932 membrane embedded and not part of a heavy metal binding domain (HMBD). This is

933 relevant, as CXXC is otherwise a pattern typically linked to a solvent-exposed metal

934 binding site in HMBDs of other P_{IB}-groups.

935
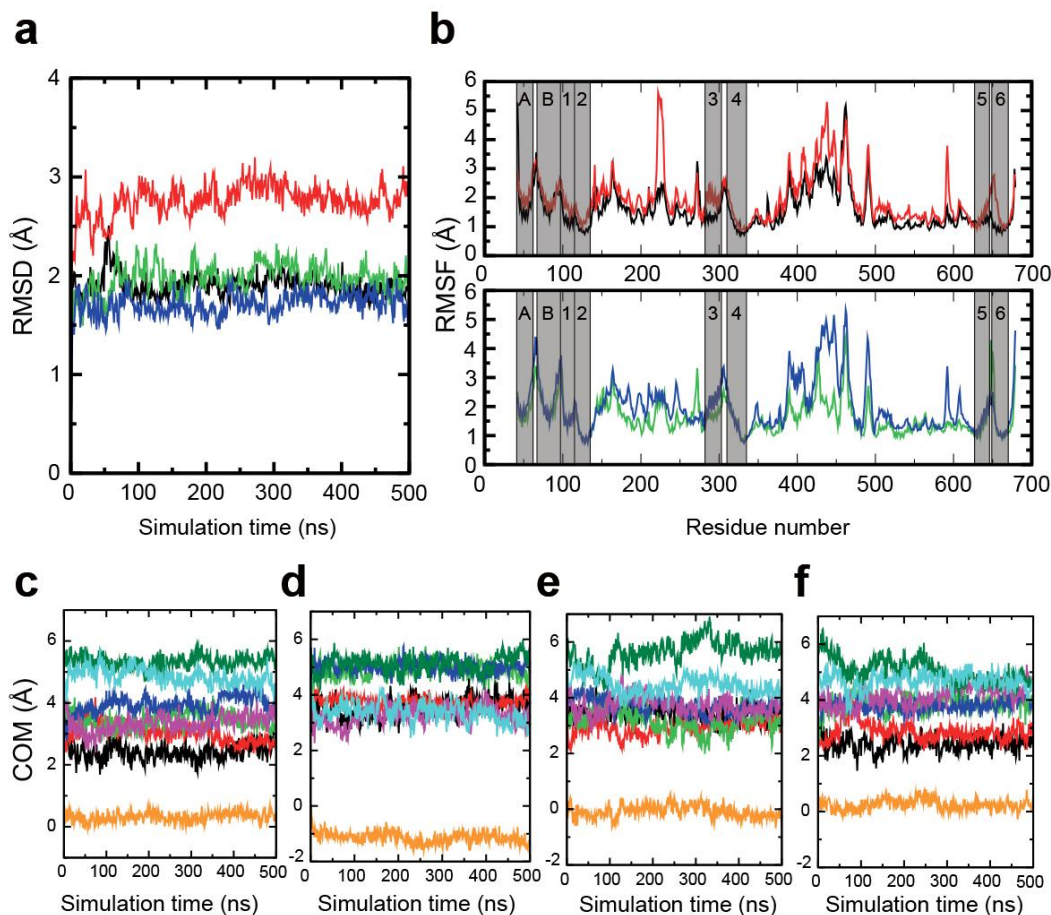
Figure 1 – figure supplement 4 │ Stability of the M-domain. Molecular dynamics
(MD) simulations were performed to assess the stability of the M-domain. **a,** Root
mean square deviation of the M-domain in AlF_4^- (black), AlF_4^--repeat (red), BeF_3^-
(green), BeF_3^--repeat (blue) simulations. **b,** RMSF of the M-domain in the AlF_4^- and
AlF_4^--repeat simulations (upper) and BeF_3^- and BeF_3^--repeat simulations (lower)
across the C_α atoms. The TM helices region are marked in transparent grey. Evolution
of the centers-of-mass of TM helices in the **c,** AlF_4^-, **d,** AlF_4^--repeat, **e,** BeF_3^-, and **f,**
BeF_3-repeat simulations. The TM helices are shown in different colors: MA (black),
MB (red), M1 (green), M2 (blue), M3 (magenta), M4 (orange), M5 (dark green) and
M6 (cyan).

a AlF$_4^-$

b AlF$_4^-$-repeat

c BeF$_3^-$

d BeF$_3^-$-repeat
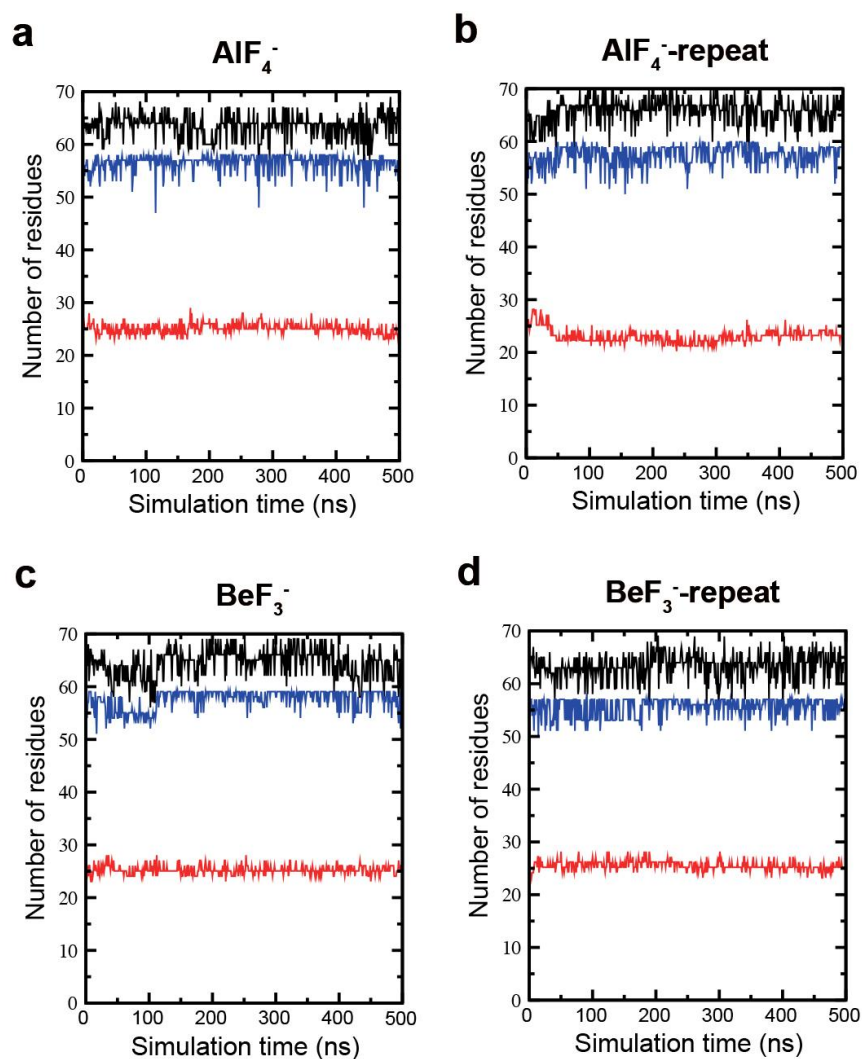
946

947 **Figure 1 – figure supplement 5 │ Secondary structure stability of the M-domain.**

948 MD simulations were performed to assess the secondary structure stability of the M-

949 domain. Total structure (black), helix (blue), and coil (red) secondary structural

950 elements in the **a,** AlF$_4^-$, **b,** AlF$_4^-$-repeat, **c,** BeF$_3^-$, and **d,** BeF$_3^-$ repeat simulations.

```
sCoaT/1-682    ..................................................................
BsZosA/1-637   ..................................................................
MtCtpD/1-657   ..................................................................
CmCzcP/1-829   MTEKLRLDIPVLLPGLPDSSDPCVERLLSELRGKEGVEAAHIKTAN.VDSDSQICVHYDP
SsZntA/1-732   .........MSTP.............DNHGKKAPQFAAFKPLTTVQNANDCCCD.G.
LpCopA/1-736   ..................................................................
```

A-domain   P-domain   N-domain   M-domain
● Ion binding aa in N-terminus   ■ Selected conserved residues

```
sCoaT/1-682    ..................................................................
BsZosA/1-637   ..................................................................
MtCtpD/1-657   ..................................................................
CmCzcP/1-829   AAISLARIRELVTSTGAVISSRFGHVLWQLKGVWHERRARTVASQLRALPGVIEAEVSAS
SsZntA/1-732   ACSSSPTLSE.......NV...SGTRYSWKVSGMDCAACARKVENAVRQLAGVNQVQVLFA
LpCopA/1-736   ..............................MKH.................................
```

                                1   10   20
```
sCoaT/1-682    ...................MRKVVAD..LNAV.......EEENMPENHTPD.......
BsZosA/1-637   ...................MNEQVIVQ....R.........
MtCtpD/1-657   ...................MTLTACEVTA.................AE.
CmCzcP/1-829   GIARVEFDNDRISAAGIEQALSKRGLAPVEIGARKSGHADHEHREGVKDHAHG.......
SsZntA/1-732   TE.KLVVDADNDIRAQVESA.......VQKAGYSLRDEQ......AAD.......
LpCopA/1-736   .........DHH...........Q.GHTHSGKGHACHHEHNSPKTQQASSKMEGPI
```

                                30   40   MA
                                                                  50
```
sCoaT/1-682    .................DGHNH...AHGGFLNRILGGRAEVIFA....VLCG
BsZosA/1-637   .................DPHEP...LKTDKRENWAQHAELIAA....LVSG
MtCtpD/1-657   .................APFDRV..SKTIPHPLSWGAALWSVVSVRWATVAL
CmCzcP/1-829   ...................EGEGH...E.AHAHGSVFGPNTELIFS....LICG
SsZntA/1-732   .................EPQ..........ASRLKENLPLITL....I
LpCopA/1-736   VYTCPMHPEIRQSAPGHCPLCGMALEPETVTVSEVVSPEYLDMRRRFWIALMLTIPV..V
```

         MA   MB   MB'   M1
         60   70   80   90   100
```
sCoaT/1-682    ICLLLGWL.GPKY.GIMSEQFGFGLLLAAYFFGGYFTLREAVEK.ISKGQFQIDFLMLVA
BsZosA/1-637   ALILAGWLLSGY......QVLSIILFLLAFVIGGFAKAKEGIEETLESKTLNVELLMIFA
MtCtpD/1-657   LLFLAG.LVAQ.L.NGAPEAMWWTLYLACYLAGGWGSAWAGAQA.LRNKALDVDLLMIAA
CmCzcP/1-829   ALLGLGFAVGKLF.GSLPAWIPVAFFVGAYFFGGFYTVREAIEN.LRLKKFEIDTLMLVA
SsZntA/1-732   VMMAISWGLEQF.....NHPFGQLAFIATTLVGLYPIARQALRLIKSGSYFAIETLMSVA
LpCopA/1-736   ILEMGGHGLKHFISGNGSSWIQLLLATPVVLWGGWPFFKRGWQS.LKTGQLNMFTLIAM.
```

         M1   M2   M3   M4
         110   120   130   140
```
sCoaT/1-682    ASGAA.......................ILGEWAEGAFLLFLFSVGHALENYAMGRARN
BsZosA/1-637   AIGSA......................LIGYWAEGAILIFISLSGALETYTMNKSSR
MtCtpD/1-657   AVGAV......................AIGQIFDGALLIVIFATSGALDDIATRHTAE
CmCzcP/1-829   AAGAA......................ALGAWAEGALLLFLFSLGHGLEHYAMGRAKR
SsZntA/1-732   AIGAL......................FIGATAEAAMVLLLFLIGERLEGWAASRARQ
LpCopA/1-736   GIGVAWIYSMVAVLWPGVFPHAFRSQEGVVAVYFEAAAVITTLVLLGQVLELKAREQTGS
```

         150   160   170   180   190   200
```
sCoaT/1-682    AVAALAGLTPDEALVRRGDKT.ETVLIENLLVGDIVVVRSNERLPADGFVVKGSSAVNQA
BsZosA/1-637   DLTSLMQLEPEEATLMVNGET.KRVPVSDLQAGDMIVIKPGERVAADGIIESGSTSLDES
MtCtpD/1-657   SVKGLLDLAPDQAVVVQGDGSERVVAASELVVGDRVVVRPGDRIPADGAVLSGASDVDQR
CmCzcP/1-829   AIEALAALAPATASVRREGEV.REVPVEELQVGDVVVVRPNERLPADGFLVKGASAVNQA
SsZntA/1-732   GVSALMALKPETATRLRNGER.EEVAINSLRPGDVIEVAAGGRLPADGKLLSPFASFDES
LpCopA/1-736   AIRALLKLVPESAHRIKEDGSEEEVSLDNVAVGDLLRVRPGEKIPVDGEVQEGRSFVDES
```

         210   220   230   240   250   260
```
sCoaT/1-682    PITGESAPVDKLPVDDPEFAAANLDKLTPQTRVFAGSINGSGSLDVQVTKLSGESTLARV
BsZosA/1-637   ALTGESMPVEKNTG................DTVFTGTVNRNGSLTVRVTKANEDSLFRKI
MtCtpD/1-657   SITGESMPVAKARG.............DEVFAGTVNGSGVLHLVVTRDPSQTVVARI
CmCzcP/1-829   PVTGESIPVDKQPVDDAAAARRKPDAVGAVSRVFAGTINGAGAIEVEVTRLSTDSALAKV
SsZntA/1-732   ALTGESIPVERATGDKVP..............AGATSVDRLVTLEVLSEPGASAIDRI
LpCopA/1-736   MVTGEPIPVAKEAS.............AKVIGATINQTGSFVMKALHVGSDTMLARI
```

                                             M3   M4
         270   280   290   300   310   320
```
sCoaT/1-682    VTLVAEAQTRQSPTQNFTKKFEKIFVPCVIALAF.VTSFSFLIL.DETAAQSFYRAMAVL
BsZosA/1-637   IKLVESAQNSVSPAQAFIERFENAYVKGVLIAVALLLFVPHFAL.GWSWSETFYRAMVFM
MtCtpD/1-657   VELVADASATKAKTQLFIEKIEQRYSLGMVAATL.ALIVIPLMF.GADLRPVLLRAMTFM
CmCzcP/1-829   VKMVNEAEAQKSPSQRFTEKFERIFVPAVLVLAV.LLLFAGLVI.NEPFSATFYRAMAVL
SsZntA/1-732   LKLIEEAEERRAPIERFIDRFSRIYTPAIMAVALLVTLVPPLLF.AASWQEWIYKGLTLL
LpCopA/1-736   VQMVSDAQRSRAPIQRLADTVSGWFVPAVILVAVLSFIVWALLGPQPQPALSYGLIAAVSVL
```

952
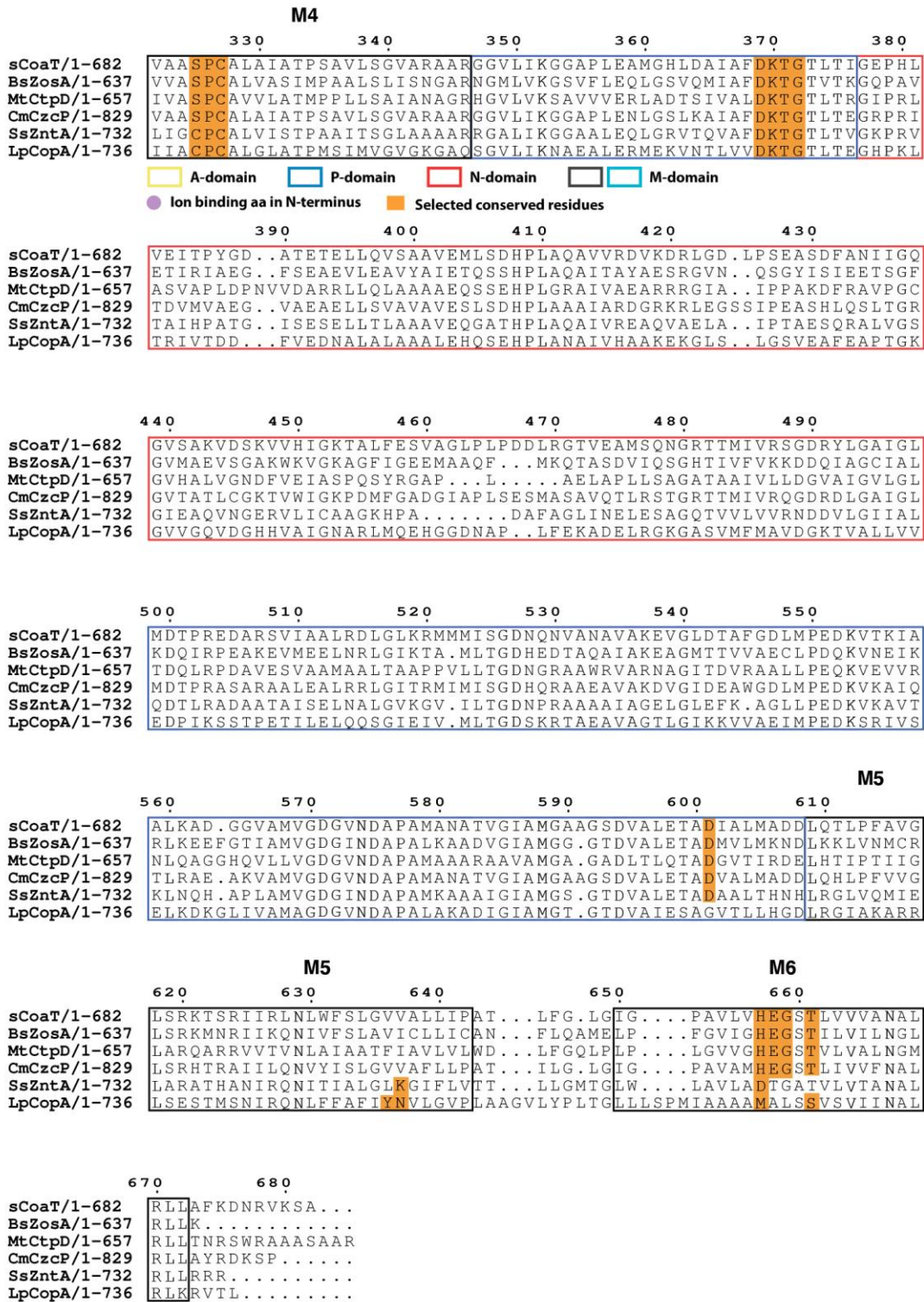
**Figure 2 – figure supplement 2 │ Sequence alignment of selected P_IB-ATPases.**
Sequence alignment of four P_{IB-4}-ATPases, sCoaT from *Sulfitobacter* sp. NAS-14.1
CmCzcP from *Cupriavidus metallidurans*, BsZoa from *Bacillus subtilis* and MtCtpD
from *Mycobacterium tuberculosis*. The P_{IB-1}-ATPase LpCopA from *Legionella*
pneumophila and the P_{IB-2}-ATPase SsZntA from *Shigella sonnei* are also included for
comparison.
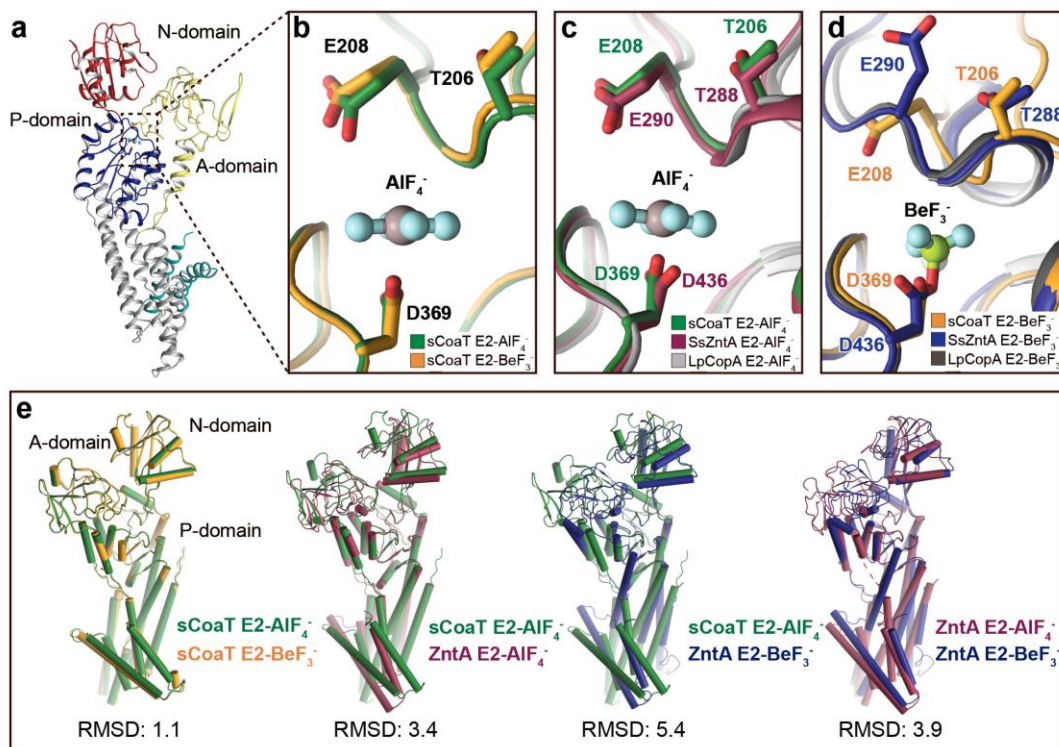
Figure 2 – figure supplement 3 │ Comparison of E2 states overall and close-views of the phosphorylation site. The TGE loop in the E2-BeF$_3^-$ stabilized sCoaT (E2P*) is pre-organised for dephosphorylation, which is not the case for SsZntA and LpCopA. **a,** The overall E2P* structure of sCoaT showing the region of focus in panels **b-d**. **b,** Comparison of the TGE loop in the two sCoaT structures, with only minor differences. **c,** Comparison of sCoaT E2.P$_i$ with the equivalent structures of SsZntA and LpCopA (PDB-ID: 4UMW and 4BYG). **d,** Comparison of sCoaT E2P* with the equivalent structures of SsZntA and LpCopA (PDB-ID: 4UMV and 4BBJ). **e,** Comparisons of E2-AlF$_4^-$ and E2-BeF$_3^-$ structures of sCoaT and SsZntA (PDB ID of SsZntA structures: 4UMV and 4UMW). All superimpositions were performed based on the P-domain, and the RMSD values based on the overall structure are listed below the structural alignments. Alignment of the E2-BeF$_3^-$ and E2-AlF$_4^-$ structures of sCoaT demonstrates that they are very similar (RMSD= 1.1), and comparison to the equivalent structures of SsZntA support the conclusion from **a-d** that both structures have been captured in occluded E2.P$_i$ transition states.

975
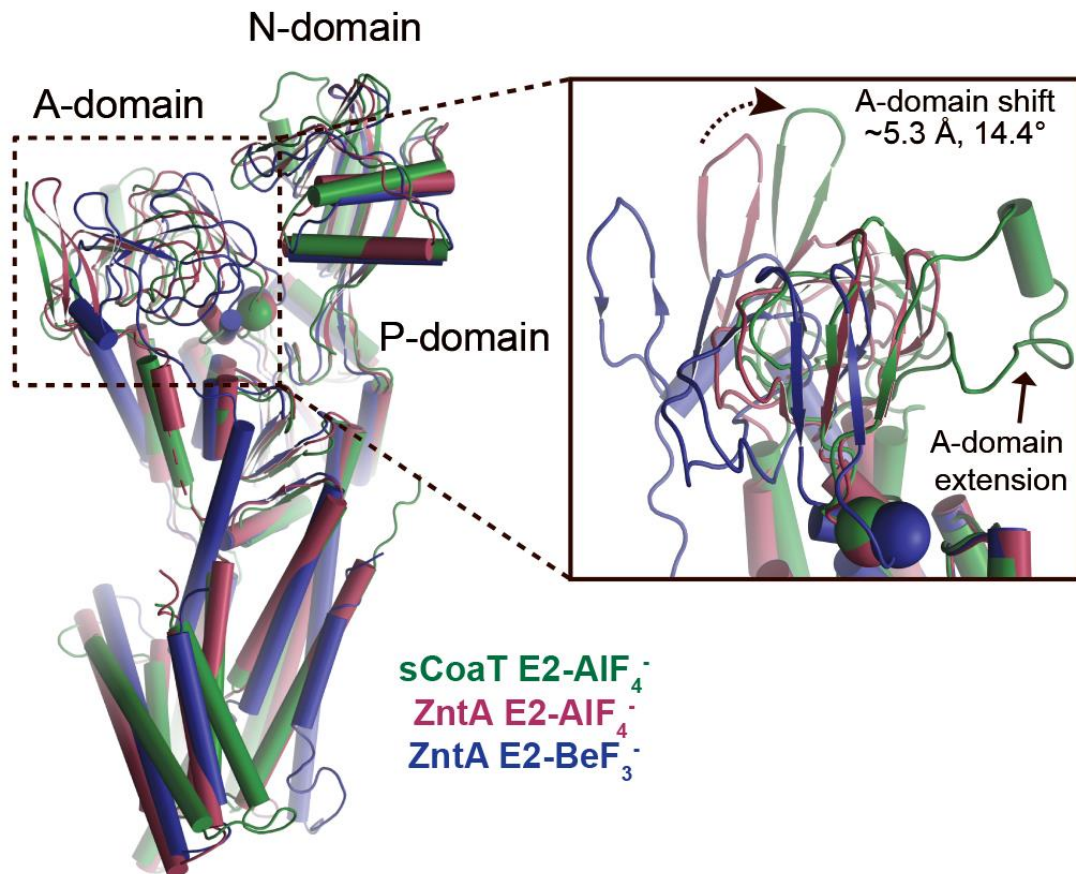
Figure 2 – figure supplement 4 │ A-domain differences. Superimposition of the
E2-AlF$_4^-$ structures of sCoaT (determined here, shown in green) and SsZntA (PDB ID
4UMW, purple) and the E2-BeF$_3^-$ structure of SsZntA (PDB ID 4UMV, blue). The
overall structures are shown to the left. The inset represents a close-view of the A-
domain, showing that the sCoaT structure is more alike the SsZntA E2-AlF$_4^-$
structure. The peripheral part of the A-domain in sCoaT is shifted closer to the P-
domain, whereas the area around the conserved TGE motif (the Glu of the TGE motif
is visualized as a sphere) superposes well with SsZntA. Like SERCA, the A-domain
of sCoaT possesses a surface-exposed extension which is however not present in P$_{IB-1}$- and P$_{IB-2}$-ATPases.